Satellite Products and Services Review Board

Algorithm Theoretical Basis Document

NOAA JPSS/VIIRS Flood Mapping (VFM) Product
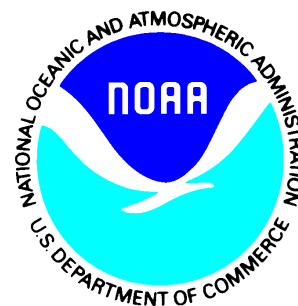
Version 1.0

June 2021

TITLE: JPSS VIIRS Flood Mapping (VFM) Algorithm Theoretical Basis Document

AUTHORS:

Sanmei Li, George Mason University

Donglian Sun, George Mason University

DOCUMENT HISTORY
DOCUMENT REVISION LOG

VIIRS Flood Mapping (VFM) Algorithm Theoretical Basis Document			
DOCUMENT CHANGE HISTORY			
Revision No.	**Date**	**Revision Originator Project Group**	**CCR Approval # and Date**
1.0	June 23, 2021	No version 1	N/A
2.0			
2.1			
2.2			

LIST OF CHANGES

Significant alterations made to this document are annotated in the List of Changes table.

VIIRS Flood Mapping (VFM) Algorithm Theoretical Basis Document					
LIST OF CHANGE-AFFECTED PAGES/SECTIONS/APPENDICES					
Version Number	Date	Changed By	Page	Section	Description of Change(s)

TABLE OF CONTENTS

Page

LIST OF TABLES AND FIGURES

1   INTRODUCTION

Floods are the most devastating, frequent, and widespread natural disaster, affecting about, on average, 80 million people per year around the world, and causing more death and property damage than any other natural phenomena (Kundzewicz and Schellnhuber, 2004; IFRC, 2008). Every year, flood disasters cause huge economic losses and social disruption all over the world (IFRC, 2008).

Because flood is a short-term event in large scale, satellite images show special advantages in flood mapping because these images can see the big pictures of floodwater with rapid update on the flood status. Thus near real-time flood mapping using satellite imagery is invaluable to river forecasters and decision-makers for disaster monitoring and relief efforts. In fact, satellite-based flood detection has a history that dates back to the 1970's. NOAA/VHRR (Very High Resolution Radiometer) and NOAA/AVHRR (Advanced Very High Resolution Radiometer) imagery served as the main data sources in flood/standing water detection prior to the development of MODIS (Moderate Resolution Imaging Spectroradiometer). Many case studies have been conducted to analyze severe flood events all over the world. These studies laid a foundation in methods and approaches of flood detection with coarse-to-moderate-resolution satellite data (Wiesnet et al., 1974; Barton and Bathols, 1989; Ali, 1989; Sheng and Xiao, 1994; Sheng et al., 1998; Sheng and Gong, 2001). Besides VHRR and AVHRR data, Landsat imagery, which are with 30-m spatial resolution, are also used in flood detection for disaster assessment and flood pattern analysis (Gupta and Bodechtel, 1982; Guptaand Banerji, 1985; Wang et al., 2002; Mueller et al., 2016; Fisher et al., 2016; Tulbure et al., 2016). Radar satellites and imagers such as Radarsat, SAR, TerraSAR-X and Sentinel-1and so on are even more popular in flood mapping because these images can penetrate cloud cover and derive flood information in cloud conditions that optical sensors fail with (Brakenridge et al., 1993; Matgenet al., 2007; Schumannet al. 2007; Martinis et al., 2009; Matgenet al., 2011; Pulvirentiet al., 2011; Martinis et al., 2013).

Although Landsat and Radar imagery demonstrate excellent capability in flood mapping, the major drawbacks of these sensors are their narrow swath width and long revisit period. Because most floods are short-term events, it is not realistic to rely on these images completely for flood mapping and management. In comparison, moderate-spatial-resolution satellites provide steadier and lower-cost data sources for near real-time flood mapping. After EOS-Terra (EOS, Earth Observing System) was launched in 1999, MODIS (Moderate Resolution Imaging Spectroradiometer) has gradually become the preferred satellite instrument for flood detection because of its daily global coverage and higher spatial resolution of the visible, near infrared (250m) and short-wave infrared (500m) channels rather than the 1km resolution channels with AVHRR (Gumley and King, 1995; Brakenridge and Anderson, 2006). Newer algorithms such as the decision-tree approach and open water likelihood method have used MODIS to more accurately detect flooding and standing water (Sun et al., 2011; Ticehurst et al., 2014; Ticehurst et al., 2015). The continuous observations from MODIS also make it possible to analyze flood inundation dynamics and generate global water mask from multiple-year detected results (Carroll, et al., 2009; Andrimont et al., 2012; Huang et al., 2014). In 2011, an experimental global flood detection system using MODIS imagery was released by NASA (National Aeronautics and Space Administration) (http://oas.gsfc.nasa.gov/floodmap). This system processes near real-time MODIS data and generates 1-day, 2-day, 3-day and 14-day composite global flood products at 10°×10° tiles from TERRA-MODIS and AQUA-MODIS (Brakenridge, 2011). The system provides systematic datasets with a robust interface to access the

products. The multiple-day composition process is applied mainly to filter cloud contamination, cloud shadows and terrain shadows, and produces multiple-day composite flood maps rather than near real-time ones. The problem with the multiple-day composition process is that some real floodwater may be lost in the composition process and it introduces a bias in the experimental MODIS flood maps. Even with the composition process, cloud shadows can persist in the MODIS flood product especially in high latitudes. More recently, the HAND (Height Above Nearest Drainage) algorithm has been applied to MODIS flood detection with better terrain shadow removal. The accuracy of MODIS flood products are still susceptible to deep terrain shadows that cannot be filtered by either multiple-day composition or HAND algorithm (Brakenridge, 2011; Liu et al., 2016).

With the launch of Suomi-NPP (SNPP) in 2012, the on-board VIIRS (Visible Infrared Imaging Radiometer Suite) sensor has many advantages over MODIS in environmental and natural disaster monitoring and analysis. VIIRS imagery has moderate spatial resolution of 375m in the visible to infrared channels, wide swath coverage of 3040km, and relatively constant resolution across the scan. These new features, especially the improved spatial resolution in the short-wave infrared channel (centering at 1.61μm) which is a key channel for flood detection, make the VIIRS data an excellent source for near real-time flood mapping. With the support from JPSS Program through a demonstration, the VIIRS flood mapping algorithm and products have been under-developed since 2013. After more than 6 years' development, the VIIRS flood mapping algorithm successfully solves the critical issues for flood automations and the products reach a level for operational production.

The VIIRS flood products, which include a VIIRS near real-time flood product, daily composited and 5-day composited flood products, are designed for the Suomi-NPP &NOA-20/VIIRS imagery to reflect flood extent in water fractions (open water percentage in a VIIRS 375-m pixel). The algorithm consists of six major processes including water detection, cloud shadow removal, terrain shadow removal, minor flood detection, floodwater fraction retrieval, and floodwater determination. The framework of the algorithm is designed to cover most of the complicated situations of water surface under different underlying conditions and geometric angles in VIIRS imagery. To provide reliable performance, floodwater is divided into supra-snow/ice water and supra-vegetation/bare land water with consideration of sun-glint contamination and salt-like clay background. Water detection is done using a combination of methods from the decision-tree technique (C4.5), threshold method, histogram method to change detection approach. Because of the similarity in spectral features among cloud shadows, terrain shadows and water surface in the visible to infrared channels, the classification methods fail to separate cloud shadows and terrain shadows from water surface, which causes severe problems for flood detection. To solve these issues, a geometry-based method is applied to differentiate cloud shadows from water pixels, and an object-based method is developed to remove terrain shadows from water pixels. Based on the water detection results, water retrieval algorithms are further applied to retrieve water fractions for supra-vegetation/bare land floodwater to derive more accurate flood extent from the 375-m VIIRS imagery. For water surface without sun-glint contamination, a dynamic nearest neighboring searching (DNNS) method is used to retrieve water fractions by considering the mixture of land types in a water pixel, and the histogram method is applied to estimate water fractions of water pixels with minor to moderate sun-glint contamination. The retrieved water fractions are compared with a water reference map generated from water layer in the 30-m National Land Cover Dataset (NLCD), the 250-m MODIS global water mask (MOD44W) and the 150-m global water bodies

from ESA's (European Space Agency) Climate Change Initiative (CCI) to determine floodwater. With the near real-time VIIRS flood detection results, daily and 5-day composited flood products are generated through a maximal water fraction composition process to derive the maximal flood extent during the periods.

This Algorithm Theoretical Basis Document (ATBD) describes in detail the procedures for developing VIIRS flood mapping algorithms and using VIIRS flood products. It includes a description of the requirements and specifications of the JPSS VIIRS flood products and some specific information about the VIIRS that is relevant to the derivation of the VIIRS Flood products. The main part of the ATBD is a description of the science of the VIIRS flood mapping algorithm, followed by the assumptions and limitations of the algorithm and products in flood detection.

1.1   Product Overview

1.1.1   Product Description

The VIIRS flood product, referred as VFM, is a newly developed product generated from Suomi-NPP and NOAA-20 VIIRS imagery to depict flood extent in floodwater fractions. Here, flood is defined as an overflow of water that submerges or "drowns" land that is normally dry. With the definition, the floodwater detected in VFM includes disastrous floodwater caused by ice-jam/snow-melting or intensive rainfall that brings about damages or economic loss, and non-disastrous floodwater such as tides, agriculture-related water and other hydrologic-activity-related water. That VFM is a newly developed product means there are no existing operational algorithms or products to inherit from the previous satellite missions or programs.

VFM includes four products: VIIRS global near real-time gridded flood product in granules from Suomi-NPP and NOA-20 between 80°S and 80°N, VIIRS near real-time gridded flood product in the NWS domains from Suomi-NPP and NOA-20, VIIRS global daily composited flood product and VIIRS global 5-day composited flood product in 136 AOIs covering the global land regions between 60°S and 75°N. Table 1-1 lists all the products produced in the operational system.

Table 1-1 VIIRS flood products produced in the operational system

Product name	Spatial resolution	Geographic Coverage	Temporal Coverage	Description
Suomi-NPP &NOAA-20/VIIRS near real-time flood product	375 m	Global land between 80° S and 80° N	DOY: 1 ~ 59, or 291 ~ 366: θ ≤85° (N), θ ≤76° (S) DOY: 60 ~ 99, or 251 ~ 290: θ ≤80° DOY: 100 ~ 250: θ ≤76° (N), θ ≤85° (S)	Reflect the current flood status at the time of the overpass
NWS regional Suomi-NPP &NOAA-20/VIIRS near real-time flood product	375 m	8 NWS domains in the CONUS and Alaska		Reflect the current flood status at the time of the overpass

| Suomi-NPP &NOAA-20/VIIRS daily composited flood product | 375 m | Global land between 60° S and 75° N in 136 AOIs | DOY: Day of Year

θ: Solar zenith angle

N: North Hemisphere

S: South Hemisphere | Reflect the daily maximal flood extent from Suomi-NPP and NOAA-20 |
| Suomi-NPP &NOAA-20/VIIRS 5-dy composited flood product | 375 m | Global land between 60° S and 75° N in 136 AOIs | | Reflect the maximal flood extent in the latest 5 days from Suomi-NPP and NOAA-20 |

1.1.2 Product Requirements

The requirements of VIIRS flood products are listed in Table 1-2.

Table 1-2 Requirements of VIIRS flood products

Product name	Formats	Latency	Measurement range	Product accuracy
Suomi-NPP &NOAA-20/VIIRS near real-time flood product	netCDF4	3 hours after an overpass arrives	Water fraction ≥25%	80% under clear-sky conditions
NWS regional Suomi-NPP &NOAA-20/VIIRS near real-time flood product	netCDF4, geotiff and shapefile	40 minutes after an overpass arrives	Water fraction ≥25%	80% under clear-sky conditions
Suomi-NPP &NOAA-20/VIIRS daily composited flood product	netCDF4, geotiff and shapefile	6 hours	Water fraction ≥25%	80% under clear-sky conditions
Suomi-NPP &NOAA-20/VIIRS 5-dy composited flood product	netCDF4, geotiff and shapefile	6 hours	Water fraction ≥25%	80% under clear-sky conditions

1.2 Satellite Instrument Description

The Visible Infrared Imaging Radiometer Suite (VIIRS) is a critical sensor on-boarding Suomi-NPP, JPSS-1 or NOAA-20 and future JPSS series, providing over 60% of all the mission data products currently defined. There are 22 spectral bands covering spectral range from 412 nm to 12 μm with nominal spatial resolution from 375 m to 750 m. Among the 22 bands, there are five Imager

bands with 375m spatial resolution in the visible (VIS) and infrared (IR) regions. The swath coverage of one scan reaches about 3040km with relatively constant spatial resolution across the scan. One particular advantage of VIIRS in comparison to other Imagers such as MODIS and AVHRR is that the short-wave infrared channel centering at $1.61\mu m$ is with spatial resolution 375 m, which provides a key channel for reliable flood detection and floodwater fraction retrieval. Because Suomi-NPP and NOAA-20 are low-orbit satellites, all these features make the VIIRS imagery an excellent data source for flood mapping. Table 1-3 lists the channel specification of the four VIIRS Imager bands used for flood mapping. [Visible Infrared Imaging Radiometer Suite (VIIRS) Sensor Data Record (SDR) User's Guide, NOAA Technical Report NESDIS 142, Washington D.C., 10 September, 2013, online at http://www.star.nesdis.noaa.gov/smcd/spb/nsun/snpp/VIIRS/VIIRS_SDR_Users_guide.pdf]

Table 1-3 Spectral specifications of VIIRS four Imager bands used for flood detection

VIIRS Bands	Central Wavelength (μm)	Bandwidth (μm)	Wavelength Range (μm)	Band Explanation	Spatial Resolution (m) at nadir
I1 (Vis)	0.64	0.08	0.60 - 0.68	Visible/ Reflective	375 m
I2 (NIR)	0.865	0.039	0.85 - 0.88	Near IR	375 m
I3 (SWIR)	1.61	0.06	1.58 - 1.64	Shortwave IR	375 m
I5 (IR)	11.45	1.9	10.5 - 12.4	Longwave IR	375 m

2 ALGORITHM DESCRIPTION

A comprehensive description of the VIIRS flood detection algorithm and data flow is presented in this section.

2.1 Processing Outline

There are six major procedures included in the VIIRS flood mapping system: Swath projection, flood detection, mosaick process, daily composition, 5-day composition and image display. Fig. 2-1 shows the system architecture and data flow. The Swath projection processes VIIRS SDR and EDR data from Suomi-NPP and NOAA-20 in the Imager bands (I-bands 01, 02, 03, 05), terrain corrected geolocation data (GITCO) and VIIRS enterprise cloud mask and projects the SDR data and EDR data into gridded granule data. The output from the swath projection process is used as the input of the flood detection process together with the ancillary datasets and outputs VIIRS near real-time flood detection results in granules for further mosaick process in the 8 NWS domains and the 136 AOIs covering global land between 60°S and 75°N. With the mosaicked data in the 136 AOIs, the daily composition composites the near real-time flood detection results and generates daily composited flood datasets from Suomi-NPP and NOAA-20. The daily composited flood datasets are further used as the input for 5-day composition process to derive VIIRS 5-day composited flood datasets. All the flood datasets are in netCDF format, and an image display process is applied on these netCDF datasets to generate VIIRS flood maps in geotiff and vector data in shapefile format.
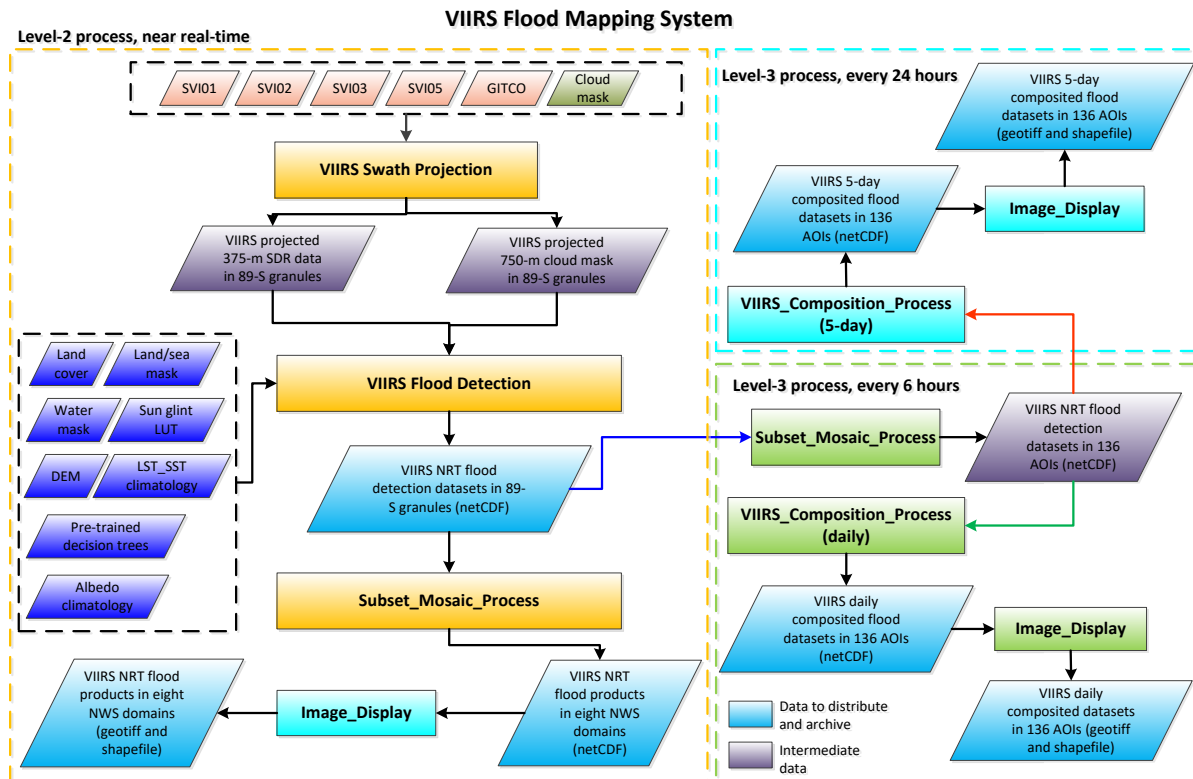
Fig. 2-1 Flowchart of VIRS flood mapping system

Among the major procedures, the VIIRS flood detection process has the core algorithm for flood mapping. The algorithm consists of six major processes including water detection, cloud shadow removal, terrain shadow removal, minor water detection, water fraction retrieval and floodwater determination. With the input data, the algorithm performs water detection using a combination of methods and approaches including decision-tree technique, threshold method, histogram method and change detection to differentiate among cloud, snow cover, river/lake ice, vegetation, bare land, supra-snow/ice water, supra-veg/bare land water without sun-glint contamination and supra-veg/bare land water with minor to moderate sun-glint contamination. Because cloud shadows and terrain shadows share similar spectral features with water surface, most shadow pixels are mixed with water pixels during the classification process. A geometry-based method is applied to remove cloud shadow pixels from water pixels, and then an object-based method is applied to remove terrain shadows pixels from water pixels. The rest water pixels are retrieved in water fractions and are used as seeds for minor water detection with change detection approach. With minor water detection, most of the water pixels with small water fractions are picked up and are applied in cloud shadow and terrain shadow removal afterward to remove potential shadow pixels. These new minor water pixels are also applied in water fraction retrieval to derive water fractions. Except supra-snow/ice water, which is used as a separate type in VIIRS flood maps, all the supra-veg/bare land water pixels are compared with water reference map to determine floodwater pixels in water fractions. Fig. 2-2 presents the process flow of VIIRS flood detection algorithm. Details of the algorithm will be presented in section 2.3.
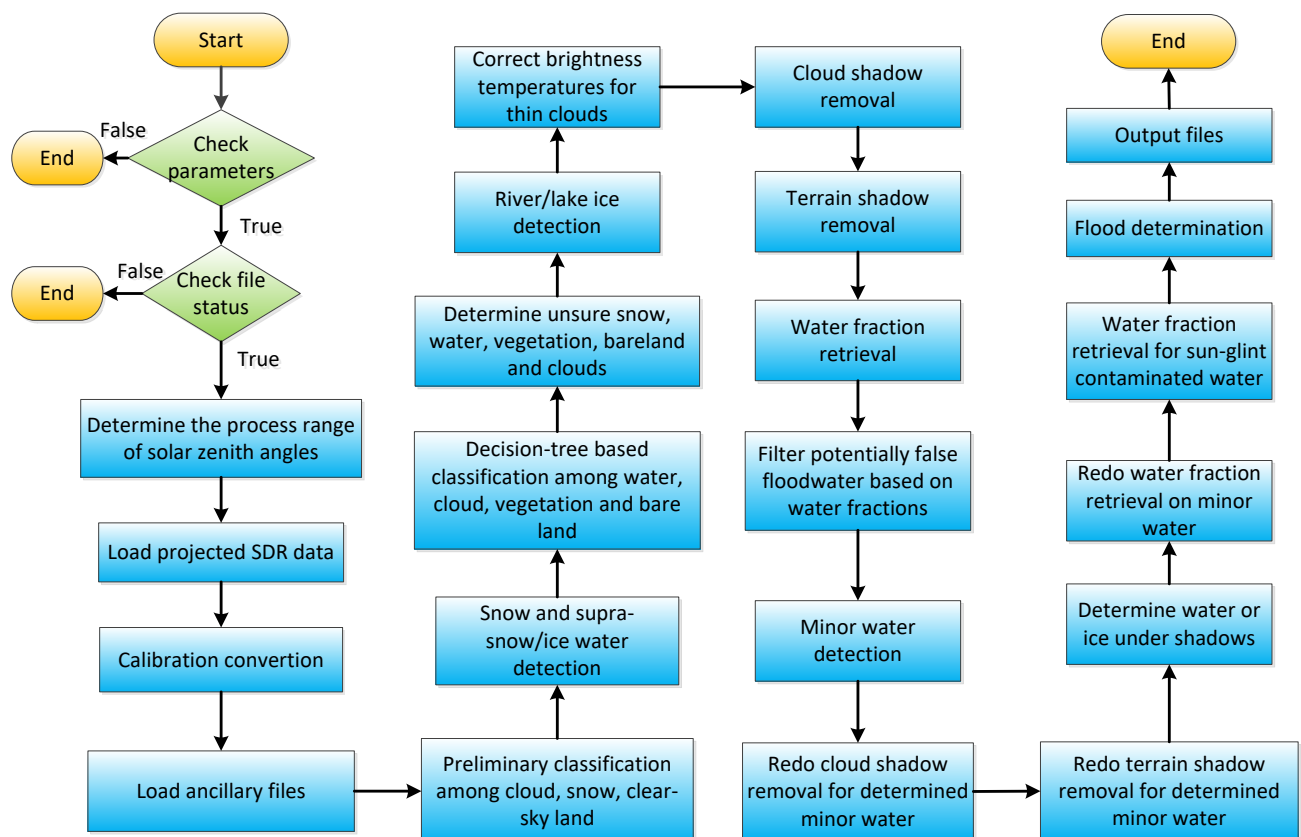
Fig. 2-2 Flow chart of VIIRS flood detection algorithm

2.2   Algorithm Input

There are three kinds of input data for the VIIRS flood detection algorithm:
• VIIRS SDR data in I-bands 01, 02 03, 05 and terrain-corrected geolocation data (GITCO);
• VIIRS level-2 enterprise cloud mask;
• Static ancillary datasets including land cover, land/sea mask, water reference mask, sun-glint lookup table, DEM, climatology of land surface temperature and sea surface temperature, albedo climatology and pre-trained decision trees.

Table 2-1 lists the specifications of VIIRS lelve-1 SDR data for flood detection, Table 2-2 shows the VIIRS lelve-2 EDR data for flood detection, and Table 2-3 lists all the static ancillary datasets used in VFM.

Table 2-1 Specifications of VFM input VIIRS SDR data

Input File	Spatial Resolution	Name Pattern	Content	Format
VIIRS Imager band 01	375m	e.g. SVI01_j01_d20200225_t1909150_e1910395_b11768_c20200226160556032790_nobc_ops	Visible channel reflectance centering at 640nm	HDF5
VIIRS Imager band 02	375m	e.g. SVI02_j01_d20200225_t1909150_e1910395_b11768_c20200226160556032790_nobc_ops	Near-infrared channel reflectance centering at 865 nm	HDF5
VIIRS Imager band 03	375m	e.g. SVI03_j01_d20200225_t1909150_e1910395_b11768_c20200226160556032790_nobc_ops	Short-wave infrared channel reflectance centering at 1.61μm	HDF5
VIIRS Imager band 05	375m	e.g. SVI05_j01_d20200225_t1909150_e1910395_b11768_c20200226160556032790_nobc_ops	Thermal infrared channel brightness temperature centering at 11.45μm	HDF5
VIIRS terrain-corrected navigation data	375m	e.g. GITCO_j01_d20200225_t1909150_e1910395_b11768_c20200226160606186943_nobc_ops.h5	Geometric angles, Geolocations	HDF5

Table 2-2 Specifications of VFM input VIIRS level-2 EDR data

Input File	Spatial Resolution	Name Pattern	Content	Format
VIIRS Enterprise Cloud Mask	750m	e.g. JRR-CloudMask_v2r1_j01_prj_s202002251909150_e202002251910395_000.h5	Cloud Mask, geolocations for Cloud Mask	NetCDF4

Table 2-3 Static ancillary datasets used by VFM

Input File	Name Pattern	Source	Format
Global land cover at 1km resolution	Global_land_cover_IGBP_2017_USGS_types.raw	VIIRS surface type in 2017 and AVHRR land cover dataset in 2000	raw
Global Digital Elevation Model at 375-m resolution	Global_DEM375m_W180_W090_N90_S90.raw, … Global_DEM375m_E090_E180_N90_S90.raw	SRTM/DEM ASTER DEM	raw
Sun-glint lookup table	Sun_Gliter_mask_005.dat	Self-support	raw
Global land/sea mask at 1km resolution	lw_geo_2001001_v03m_1km.raw		raw
Global water mask	VIIRS_Global_MOD44W_Water_Mask.raw	MOD44W, ESA's global water mask, NLCD 2006	raw
Land/sea surface temperature 16-day climatology at 5km resolution	AQUA_Daytime_LST_SST_Climatology_NNN.raw	MODIS LST/SST	raw
Global Albedo monthly climatology at 5km resolution in visible channel	CMG-SMT-P0B1_ch1_{Channel number}.raw	MODIS Albedo dataset	raw
Pre-trained decision trees and tree attribute files	Tree_{tree number}_attr.txt Tree{tree number}_J48graft_{description}.txt	Self-support	txt

User AOI definition file: to list the geographic information of each subset	User_AOI_Definition.txt	User defined	txt

2.3 Theoretical Description

2.3.1 Physical Description

2.3.1.1 Physical basis for water detection

Water detection using optical satellite data is primarily based on the spectral features of water surface in visible (Vis, centering at 650nm), near-infrared (NIR, centering at 865 nm) and short-wave infrared (SWIR, centering at 1610nm) channels (Wiesnet et al., 1974; Barton, 1989; Sheng and Xiao, 1994).

Without sun-glint contamination, the water surface has overall low reflectance in the Vis, NIR and SWIR channels. Compared to cloud and snow/ice, the reflectance of water surface in the Vis and NIR channels are much lower, which can be used as a primary feature to differentiate water from cloud and snow/ice in optical satellite imagery. Although the reflectance difference between water surface and vegetation or bare soil is much smaller, the spectral features in the Vis, NIR and SWIR channels can still be used to discriminate one from another. As shown in Fig. 2-3, water has higher reflectance in Vis channel than in NIR and SWIR channels. Vegetation is more reflective in the NIR channel than in Vis channel. Reflectance of bare land increases with increasing wavelength, with a maximum in SWIR channel, whereas the reflectance of water is close to 0 in this channel (Li et al., 2017).
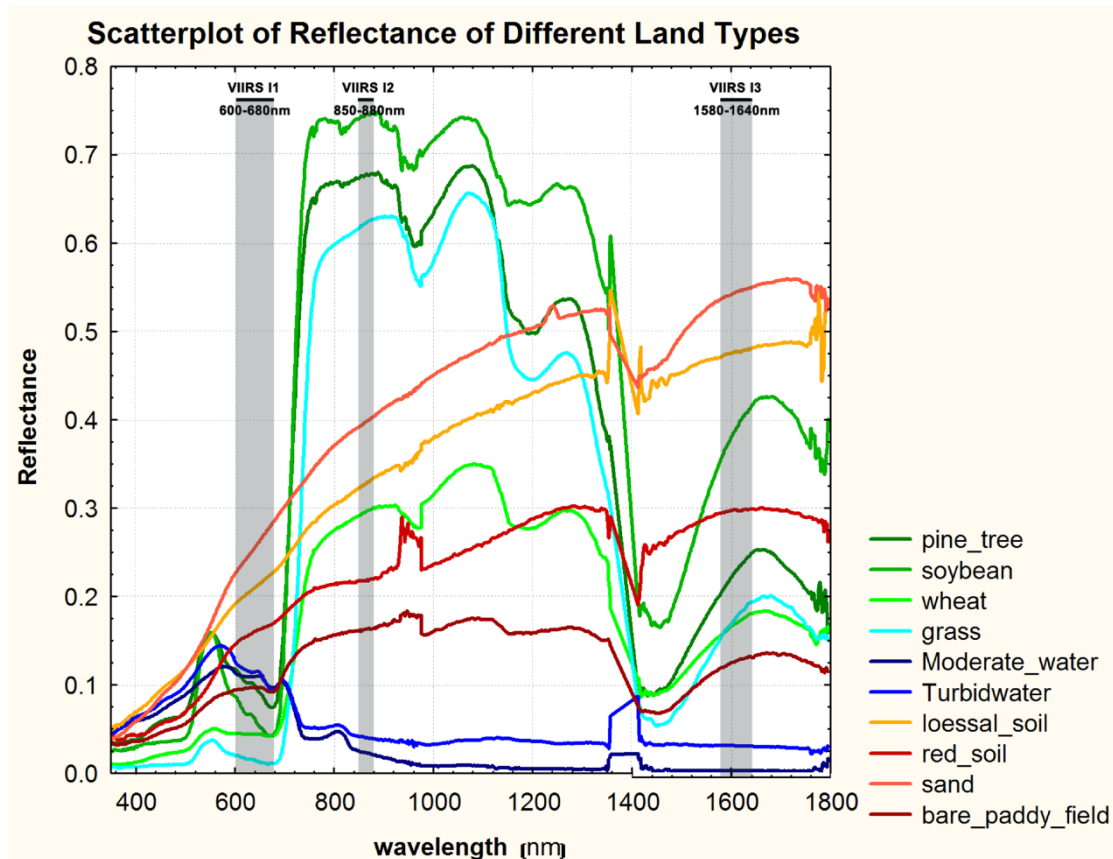
Fig. 2-3 Plot of reflectance of different land types from VIS to SWIR band range (Li et al., 2012)

With sun-glint contamination, however, the reflectance of water surface in the Vis, NIR and SWIR channels can be quite different, depending on how severe the sun-glint contamination is. More sun-glint contamination generally results in higher reflectance, especially in the NIR and SWIR channels (Cox, C., Munk, 1954; Montagner F, Billat V, Bélanger S, 2003). With minor to moderate sun-glint contamination, the reflectance of water surface in these channels is higher but still shows similar spectral patterns to non-sun-glint contaminated water surface in optical satellite imagery, and thus is detectable. Nevertheless, under severe sun-glint contamination, the reflectance of water surface is quite high, with the severest resulting in saturate spectral response from optical sensors in these channels, which makes it difficult to be differentiated from other types in satellite imagery.

Although the spectral features of water surface in Vis, NIR and SWIR channels provide primary physical basis for water detection, the situation can be much more complicated in optical satellite imagery with moderate spatial resolution. This is because many floodwater pixels in moderate-resolution satellite imagery are a mixture of water, vegetation, bare soil, snow/ice and/or other land types. Suspending matter contained in water and the underlying conditions of water can affect the water signals received by sensors as well, resulting in different spectral features in different situations. Floodwater with vegetation and bare soil background or mixture (called supra-veg/bare land flood) shows blended spectral features with water and vegetation or bare soil. In comparison, floodwater with snow/ice background or mixture (called supra-snow/ice flood) demonstrates blended

spectral features with water and snow/ice, which is quite different to supra-veg/bare land floodwater. The mixture feature of floodwater weakens water signals and the blended spectral properties make it difficult to discriminate floodwater from other land types especially from muddy land, cloud shadows and terrain shadows based on spectral characteristics.

Although the reflectance of water in the Vis, NIR and SWIR channels varies with flood types, the reflectance in most situations still keeps a similar pattern with higher reflectance in the Vis channel than in NIR and SWIR channels. Therefore, indices such as NDVI (Normalized Difference Vegetation Index), NDSI (Normalized Difference Snow Index) and NDWI (Normalized Difference Water Index) can be more steadier and thus are quite effective in water detection (Rouse, et al., 1965; Sellers 1985; Xiao, et al., 2001; Gao, 1996; Ceccato, et al., 2002). NDVI, NDSI and NDWI are defined as follows:

$$\text{NDVI} = \frac{R_{NIR} - R_{Vis}}{R_{NIR} + R_{Vis}} \tag{2-1}$$

$$\text{NDSI} = \frac{R_{Vis} - R_{SWIR}}{R_{Vis} + R_{SWIR}} \tag{2-2}$$

$$\text{NDWI} = \frac{R_{NIR} - R_{SWIR}}{R_{NIR} + R_{SWIR}} \tag{2-3}$$

In Equations (2-1) through (2-3), R_{Vis} is reflectance in Vis channel, R_{NIR} is reflectance in NIR channel, and R_{SWIR} is reflectance in SWIR channel. These indices show similar to or even better discrimination capability in water detection than R_{Vis}, R_{NIR} and R_{SWIR}. However, none of these indices differentiates floodwater from other land types independently. Instead, the combination of these variables is the basis of a robust flood detection technique. Fig. 2-4 presents six scatter plots of vegetation, bare land, water and cloud shadow from these six variables from 1-km NOAA-17/AVHRR images. From Fig. 2-4, all the variables show capability in differentiating water from vegetation and bare land to different extent, and thus can be used for water detection. However, none of them differentiates water from other types independently. One particular thing to mention in Fig. 2-4 is that most of the cloud shadow samples are mixed with water samples in all the plots, indicating similar spectral features between the two and difficulty to differentiate one from the other by using these six variables.
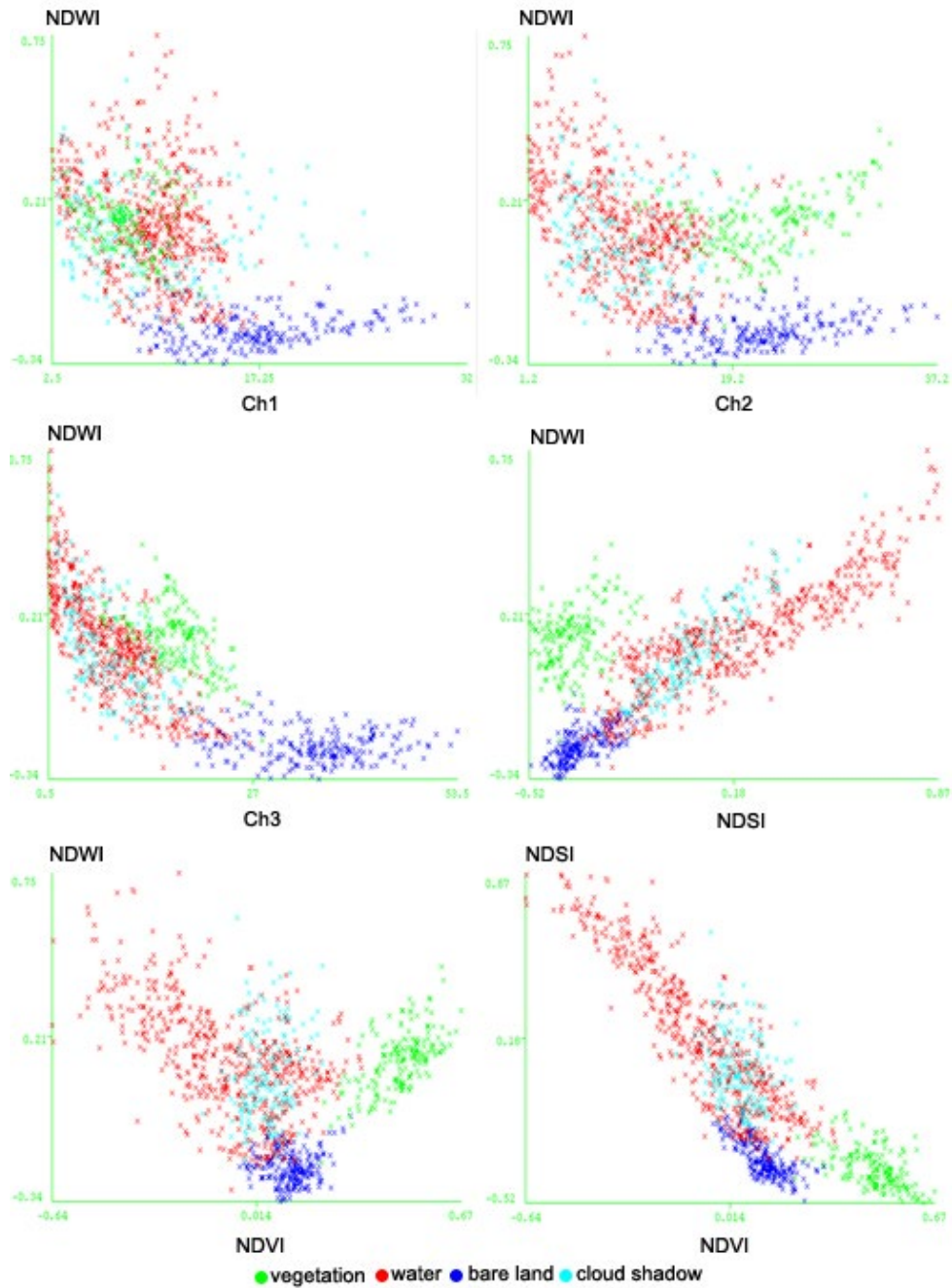
Fig. 2-4 Scatter plots of vegetation, water, bare land and cloud shadow in Vis (ch1), NIR (Ch2) and SWIR (Ch3) from NOAA-17/AVHRR

2.3.1.2 Physical description for cloud shadow removal

Cloud shadow is cast by clouds on the ground or over other lower clouds. The shadowed area is typically darker than the non-shadowed area because of less irradiance, which makes it look alike floodwater in optical satellite imagery. As mentioned in section 2.3.1.1, because of the mixture

feature of floodwater, it is difficult to differentiate floodwater from cloud shadows based on its spectral characteristics. Instead of spectral means, one feasible way to remove cloud shadows in optical satellite imagery is geometry-based method (Li et al, 2013; Khlopenko and Trishchenko, 2007).

The physical basis to remove cloud shadows geometrically is to construct the relationship among the sun, satellite, cloud, and cloud shadow. The construction of the geometry relationship involves with the calculation of parallax distance and shadow length, which can be described using viewing point (V), object (O) and light source (S) in Fig. 2-5. A parallax is the apparent displacement or difference in the position of an object viewed along two different lines of sight and is measured by the angle or semi-angle of inclination between those two lines. As shown in Fig. 2-5, when viewing an object O with height h from different viewing points (V and V_1), the position of O is located at different points (P and P_{O1}) in the image plane, where P is the position obtained from a vertical viewing angle and represents the exact position of O without parallax. When O is viewed from point V_1 at elevation angle θ_V, the corresponding position of O in the image plane is P_{O1} instead of P. The displacement from P to P_{O1} is an example of parallax. The distance between PO_1 and P is the parallax distance, which can be measured using the object's height and elevation angle.

When an opaque object comes between an area and a source of radiation, thereby intercepting radiation to the area, a shadow occurs. Shadows can be viewed as a type of parallax if the light source is considered as a viewing point, and thus shadow length is calculated in a similar way to parallax distance. As shown in Fig. 2-5, when light source (S) has an elevation angle θ_S, line object PO with height h casts its shadow along line PS_O. The shadow position of O locates at S_O. The shadow length PS_O can be calculated from the object height and light source elevation angle.
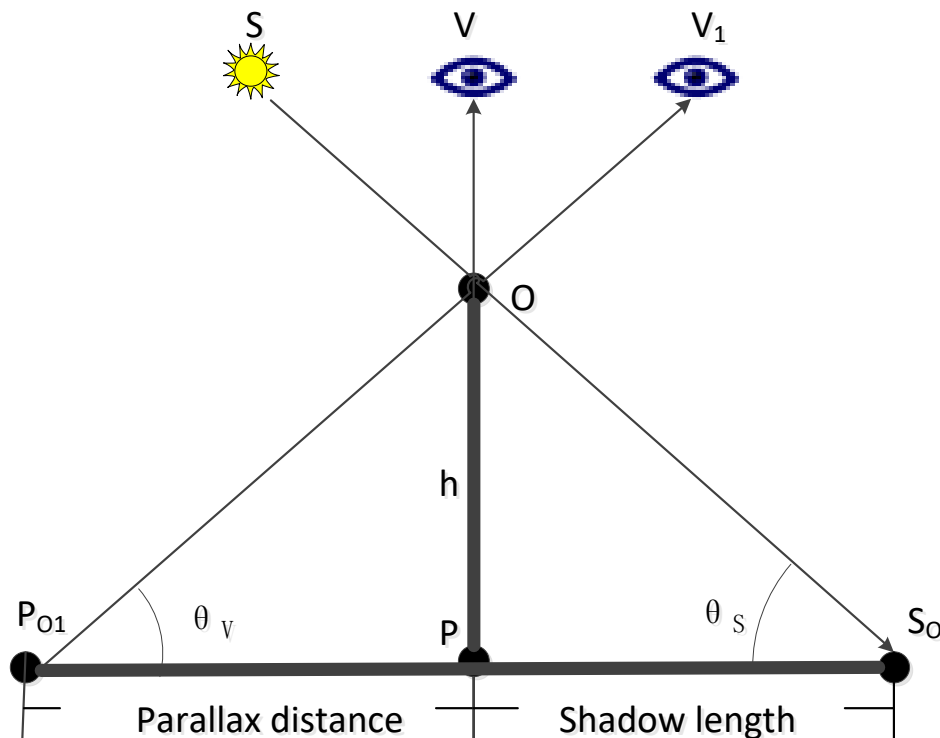
Fig. 2-5 Graph of parallax and shadow

If the relationship shown in Fig. 2-5 is extended to an ideal plane, the relationship among the sun, cloud, cloud shadow and satellite can be constructed if the earth surface is considered as ideal plane. Fig. 2-6 shows a sketch of this geometry relationship, and the position of shadow point S_{O1} ($X_{S_{O1}}$, $Y_{S_{O1}}$) in the image plane can be expressed in equations (2-4) and (2-5):

$$X_{S_{O1}} = X_{O_1} + \frac{h}{\tan \theta_v * r} * \sin \varphi_v - \frac{h}{\tan \theta_s * r} * \sin \varphi_s \qquad (2\text{-}4)$$

$$Y_{S_{O1}} = Y_{O_1} - \frac{h}{\tan \theta_v * r} * \cos \varphi_v + \frac{h}{\tan \theta_s * r} * \cos \varphi_s \qquad (2\text{-}5)$$

Where, θ_v is the sensor viewing elevation angle, φ_v is the sensor viewing azimuth angle, θ_s is the solar elevation angle, φ_s is the solar azimuth angle, r is spatial resolution, h is cloud height, and (X_{O_1}, Y_{O_1}).is the position of cloud in satellite imagery.
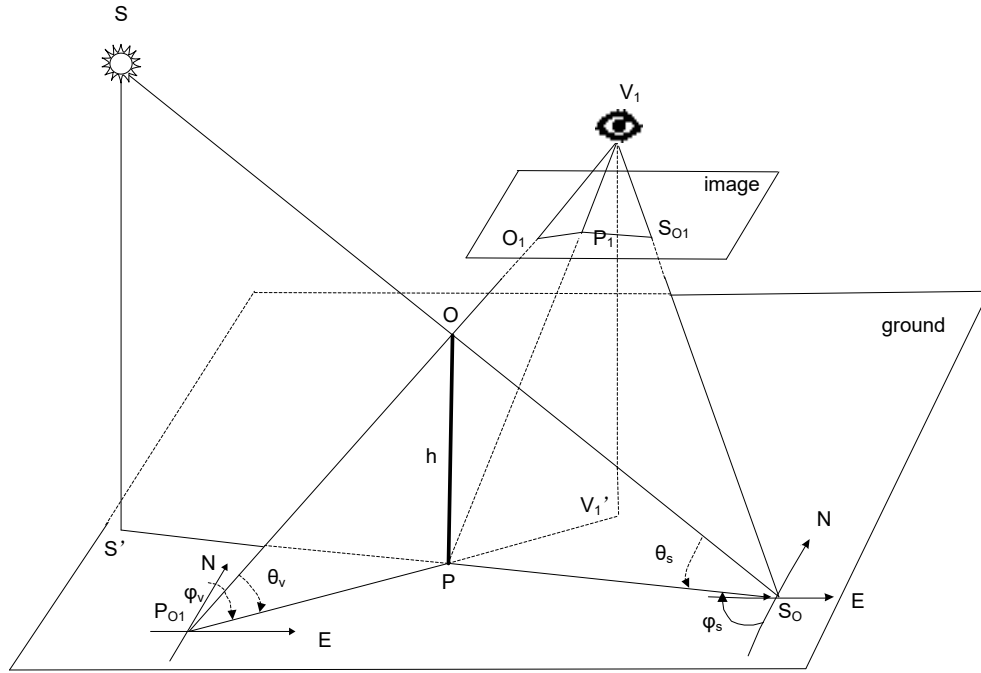
Fig. 2-6 Sketch of geometry relationship over ideal plane among the sun, cloud, cloud shadow and satellite

The geometry relationship over spherical plane is more complex by considering the curvature of earth surface. The sketch of this model is presented in Fig. 2-7. In Fig. 2-7, if the position of a cloud pixel B (lon_B,lat_B) in satellite imagery is known, the position of that cloud pixel P(lon_P,lat_P) can be located by calculating an inverse cosine function of sensor azimuth angle φ_B.

$$lat_P = \sin^{-1}[\sin(lat_B) \times \cos\frac{\widehat{PB}}{R} + \cos(lat_B) \times \sin\left(\frac{\widehat{PB}}{R}\right) \times \cos\varphi_B] \quad (2\text{-}6)$$

$$lon_P = lon_B + \tan^{-1}[\frac{\sin\varphi_B \times \sin\frac{\widehat{PB}}{R} \times \cos(lat_B)}{\cos\frac{\widehat{PB}}{R} - \sin(lat_B) \times \sin(lat_P)}] \qquad (2\text{-}7)$$

The Earth's radius is R and the arc $\widehat{PB}$ is the parallax distance between real cloud position P and cloud position in satellite imagery B.

With the cloud position P(lon_P,lat_P), cloud shadow position A (lon_A, lat_A) in satellite imagery can be calculated with solar azimuth angle φ_P by considering shadow length $\widehat{PA}$.

$$lat_A = sin^{-1}[sin(lat_P) \times cos\frac{\widehat{PA}}{R} + cos(lat_P) \times sin\left(\frac{\widehat{PA}}{R}\right) \times cos\varphi_P] \qquad (2\text{-}8)$$

$$lon_A = lon_P + tan^{-1}[\frac{sin\,\varphi_P \times sin\frac{\widehat{PA}}{R} \times cos(lat_P)}{cos\frac{\widehat{PA}}{R} - sin(lat_P) \times sin(lat_A)}] \qquad (2\text{-}9)$$

In Equations (2-6) through (2-9), $\widehat{PA}$ and $\widehat{PB}$ can be calculated as arcs in a circle with radius R using shadow angle α and parallax angle β respectively. The shadow angle α and parallax angle β are derived using Equation (2-10):

$$\delta = cos^{-1}\left[\frac{(R+h)^2 - (\sqrt{R \times R \times cos^2\theta + h \times (h+2R)} - R \times cos\,\theta)^2 + R^2}{2.0 \times R \times (R+h)}\right] \qquad (2\text{-}10)$$

Where, δ represents shadow angle α or parallax angle β, R is Earth's radius, h is cloud height, and θ is zenith angle.

In contrast, if shadow position A (lon_A, lat_A) is known, then Equations (2-6) through (2-10) can also be used to predict cloud position B (lon_B, lat_B) on the spherical surface in satellite imagery. Thus, based on the geometry relationships among the sun, cloud, cloud shadow and satellite, the positions of cloud shadows can be predicted in the VIIR imagery.
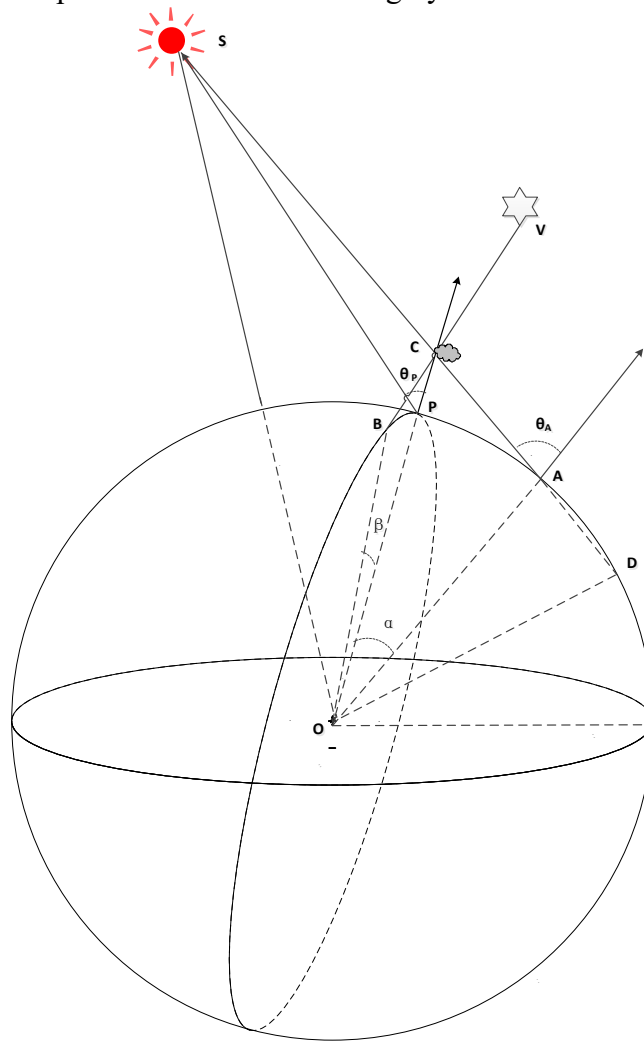
Fig. 2-7 Sketch of geometry model over spherical plane

2.3.1.3　　Physical description for terrain shadow removal

Similar to cloud shadows, most terrain shadows cannot be differentiated from floodwater based on spectral features because of their spectral similarity in the Vis, NIR and SWIR channels. Because terrain shadows are formed due to the obstacle of solar radiation by surrounding higher topography, they always appear in mountainous areas with large surface roughness. Different to terrain shadows, due to water's fluid feature, floodwater generally accumulates in low-lying areas with small surface roughness. Therefore, surface roughness can be an effective variable to differentiate between terrain shadows and floodwater.

The most straightforward variable to describe surface roughness is root-mean-square (RMS) height (γ), which is expressed in Equation (2-11) (Shepard et al., 2001):

$$\gamma = \left(\frac{1}{n-1}\sum_{i=1}^{n}(z_i - \bar{z})^2\right)^{\frac{1}{2}} \tag{2-11}$$

Where n is the number of sample points, z_i is the height of the surface at point i, and $\bar{z}$ is the mean height of the profile over all points.

Other variables including the internal height difference (referred as D_{mean}) between the higher surface mean height $\bar{Z}_{\text{h}}$ and the lower surface mean height $\bar{Z}_{\text{l}}$, and the external height difference (referred as D_{n}) between the mean height of neighboring non-shaded or non-flooding land pixels $\bar{Z}_{\text{land}}$ and the mean height of terrain shadow or floodwater pixels $\bar{Z}$, are also effective for surface roughness expression. D_{mean} and D_{n} are calculated in Equations (2-12) and (2-13), respectively:

$$D_{\text{mean}} = \bar{Z}_{\text{h}} - \bar{Z}_{\text{l}} \tag{2-12}$$
$$D_{\text{n}} = \bar{Z}_{\text{land}} - \bar{Z} \tag{2-13}$$

Fig. 2-8, Fig. 2-9 and Fig. 2-10 show the histogram plots of γ, D_{mean} and D_{n} between terrain shadows and floodwaters. From Fig. 2-8 to Fig. 2-10, terrain shadows show much larger surface roughness than floodwaters in these three variables, which provide the physical basis for terrain shadow removal.
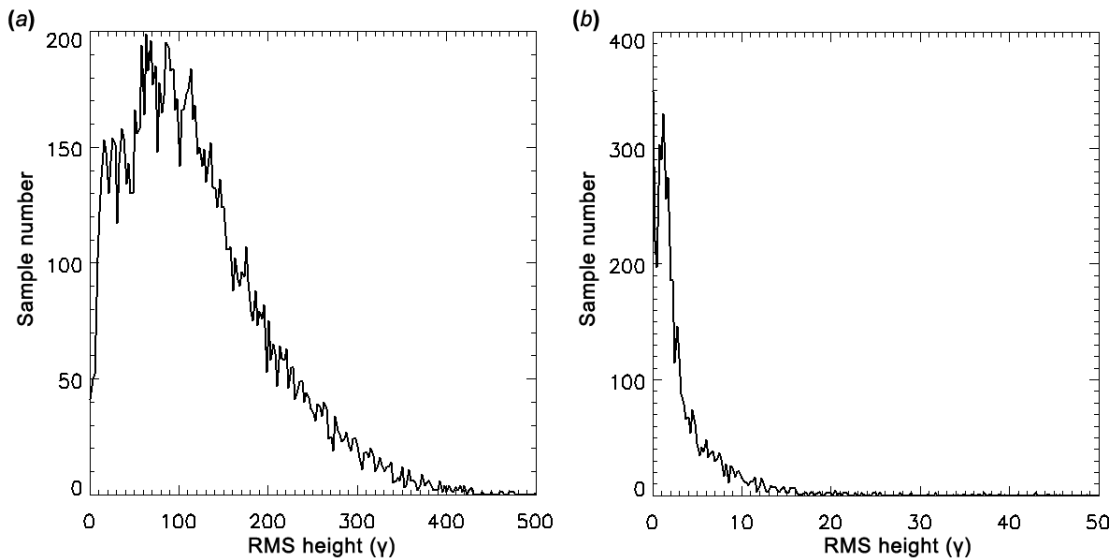
Fig. 2-8 (*a*) Histogram plot of RMS height (γ) on terrain shadows; (*b*) Histogram plot of RMS height (γ) on floodwaters
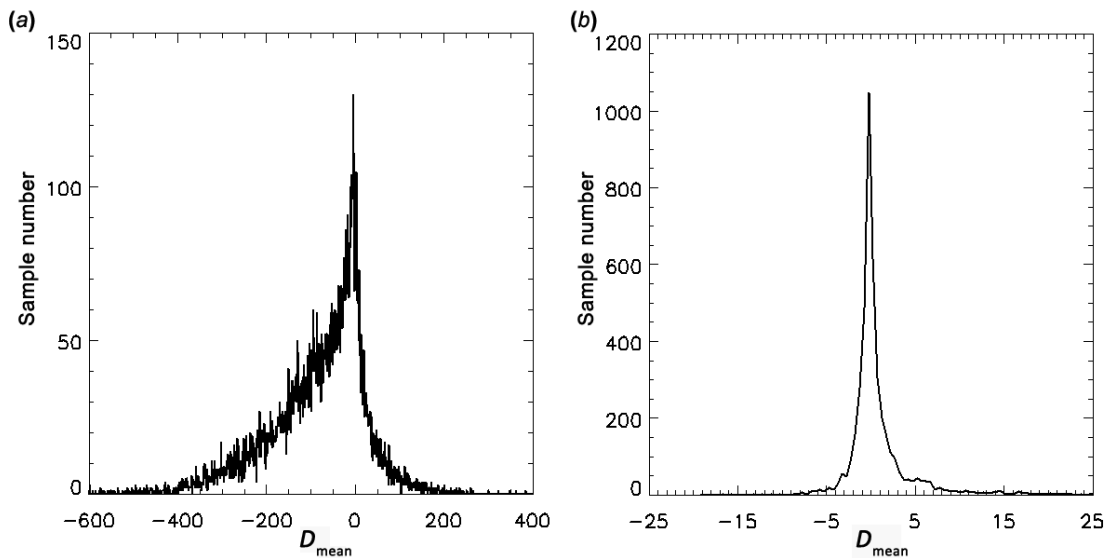
Fig. 2-9 (a) Histogram plot of D_{mean} on terrain shadows; (*b*) Histogram plot of D_{mean} on floodwaters
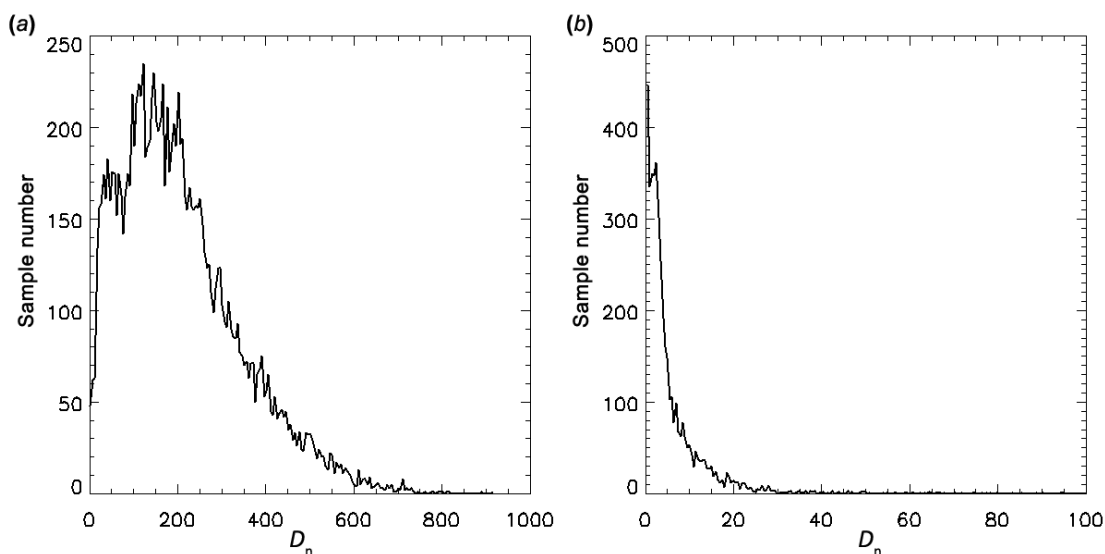
Fig. 2-10 (*a*) Histogram plot of D_n on terrain shadows; (*b*) Histogram plot of D_n on floodwaters

2.3.1.4 Physical description for water fraction retrieval

For flood mapping with moderate-spatial-resolution satellite images, water fractions represent flood extent more accurately than water/no water masks. Therefore, the VFM retrieves water fractions for supra-veg/bare land floodwater, which is the most common flood type, to derive more accurate flood extent. Linear combination model based on multispectral linear mixture theory is the

general way for sub-pixel fraction retrieval in optical satellite imagery (Sheng et al, DeFries et al., and Jiang et al.). Based on the theory, the reflectance of a mixed water pixel combined with different land types in the visible to the SWIR channels can be expressed as:

$$R = \sum_{i=1}^{n} f_i * R_i \qquad (2\text{-}14)$$

Where, R is total pixel reflectance, R_i is the reflectance of a land type with fraction f_i.

Based on Equation (2-14), water fraction can be expressed in Equation (2-15):

$$f_w = \frac{R_{ch\_land} - R_{ch\_mix}}{R_{ch\_land} - R_{ch\_water}} \qquad (2\text{-}15)$$

In Equation (2-15), f_w represents the fraction of water, R_{ch_mix} is the observed reflectance of a mixed pixel (comprised of water and land), R_{ch_land} is the reflectance of land with similar mixture to the sub-pixel land component, and R_{ch_water} is the reflectance of a water pixel with similar water type to the sub-pixel water component.

For supra-veg/bare land floodwater without sun-glint contamination, due to the low reflectance of water surface in the Vis, NIR and SWIR channels comparing to the land, the sub-pixel land portion poses strong impact on water fraction retrieval. From Fig. 2-3, because different land types reflect differently, different mixture of land types show different mixed reflectance and thus affect the radiance of sub-land portion significantly. Therefore, the mixture structure of land types should be considered during water fraction retrieval. Different to supra-veg/bare land floodwater without sun-glint contamination, the signals from water portion of floodwater with minor to moderate sun glint contamination are much stronger in comparison to the land portion and the impact from the variety of land mixture structure in the sub-pixel land portion is relatively small and may be ignored.

Among the Vis, NIR and SWIR channels, the reflectance of water surface in the SWIR channel is close to 0 and is much less variable with suspending matter and observing angles than the other two channels. This channel may be an ideal channel for water fraction calculation.

2.3.2   Mathematical Description

2.3.2.1   Water Detection

2.3.2.1.1   Cloud and snow/ice masking

The VFM uses VIIRS enterprise cloud mask to help mask cloud cover, but does not all depend on it. Instead, the VFM has cloud detection capability. The algorithm detects cloud first and then compares its cloud detection results with VIIRS cloud mask to confirm cloud cover and detection quality. For cloud detection, the VFM uses variables including R_{Vis}, R_{NIR}, R_{SWIR}, NDVI, NDSI, NDWI and T_{ch5} (brightness temperature in I-band 05 centering at 11.45µm) to do a preliminary classification based on Mahalanobis Distance and threshold classification methods on desert and non-desert land types, which clusters pixels into three types: cloud, snow/ice and clear-sky land. This step differentiates most thick cloud cover that can be easily determined from other types, and the rest cloud cover may be included in snow/ice and clear-sky land. A snow/ice detection algorithm

based on the variables R_{Vis}, R_{NIR}, R_{SWIR}, NDVI, NDSI, and T_{ch5} along with the ancillary datasets including land cover, land/sea mask, DEM, SST and LST climatology and albedo climatology, is then applied to further differentiate among cloud, snow/ice cover and clear-sky land. This step discriminates snow/ice cover and cloud cover counted in snow/ice during the first step. The rest cloud cover pixels, most of which are thin cloud and fractional cloud, are determined in the next water detection step based on decision-tree technique, threshold method and change detection approach. The final detected cloud cover is compared with VIIRS enterprise cloud mask to further confirm cloud cover. The detection quality is defined as:

A pixel is defined in high-quality detection if it meets either of the following situations:
1) It is detected as cloud in VFM and shows as confident cloud in VIIRS cloud mask;
2) It is detected as non-cloud in VFM and shows as confident clear-sky in VIIRS cloud mask.
A pixel is defined in low-quality detection if it meets either of the following situations:
1) It is detected as cloud in VFM but shows as a confident clear-sky pixel in VIIRS cloud mask;
2) It is detected as non-cloud in VFM but shows as confident cloudy in VIIRS cloud mask.

2.3.2.1.2 Supra-snow/ice water detection

Supra-snow/ice water detection is an additional step of snow/ice because most supra-snow/ice water is counted as snow/ice cover by VFM's snow/ice detection algorithm. Unlike water with vegetation and bare land background, floodwater with a background of snow/ice reflects much higher in Vis and NIR channels due to the mixture of snow/ice signals, but keeps the feature with higher reflectance in the Vis channel than in the NIR channel (Liang et al., 2012; Johansson and Brown, 2013; Lesson et al, 2013). Because snow/ice and water reflect similarly in the SWIR channel, the detection of supra-snow/ice water mainly depends on variables: R_{Vis}, R_{NIR} and NDVI. Melting snow/ice surface and shadows cast on snow/ice surface can be easily confused with supra-snow/ice water because of similar spectral features in these three variables. To solve this problem, a new DNDVI variable is defined as the NDVI difference between a pixel and the surrounding snow/ice cover. With similar R_{Vis} and R_{NIR}, a melting snow surface and shadows cast on a snow surface have smaller negative DNDVI than supra-snow/ice water. Fig. 2-11 presents four scatter plots, collected from about 50 VIIRS granules mainly in Alaska during spring break-up seasons in 2014, 2015 and 2016, of supra-snow/ice floodwater (black), shadows over snow surface (blue) and melting snow surface (red). The relationship between R_{Vis} and NDVI is in Fig. 2-11 (a). Fig. 2-11 (b) compares R_{NIR} with NDVI, scatter plot between R_{Vis} and DNDVI is shown in Fig. 2-11 (c), and Fig. 2-11(d) shows R_{NIR} and DNDVI. Fig. 2-11 illustrates that shadows on snow surfaces and melting snow surfaces have similar values in the three variables: R_{Vis}, R_{NIR} and NDVI, and overlap with the scatter plot of supra-snow/ice water (Fig. 2-11 (a) and Fig. 2-11 (b)). However, with DNDVI, the populations of melting snow samples and shadow samples separate from supra-snow/ice water samples (Fig. 2-11 (c) and Fig. 2-11 (d)). Based on this feature, the combination use of these four variables provides effective supra-snow/ice water detection.
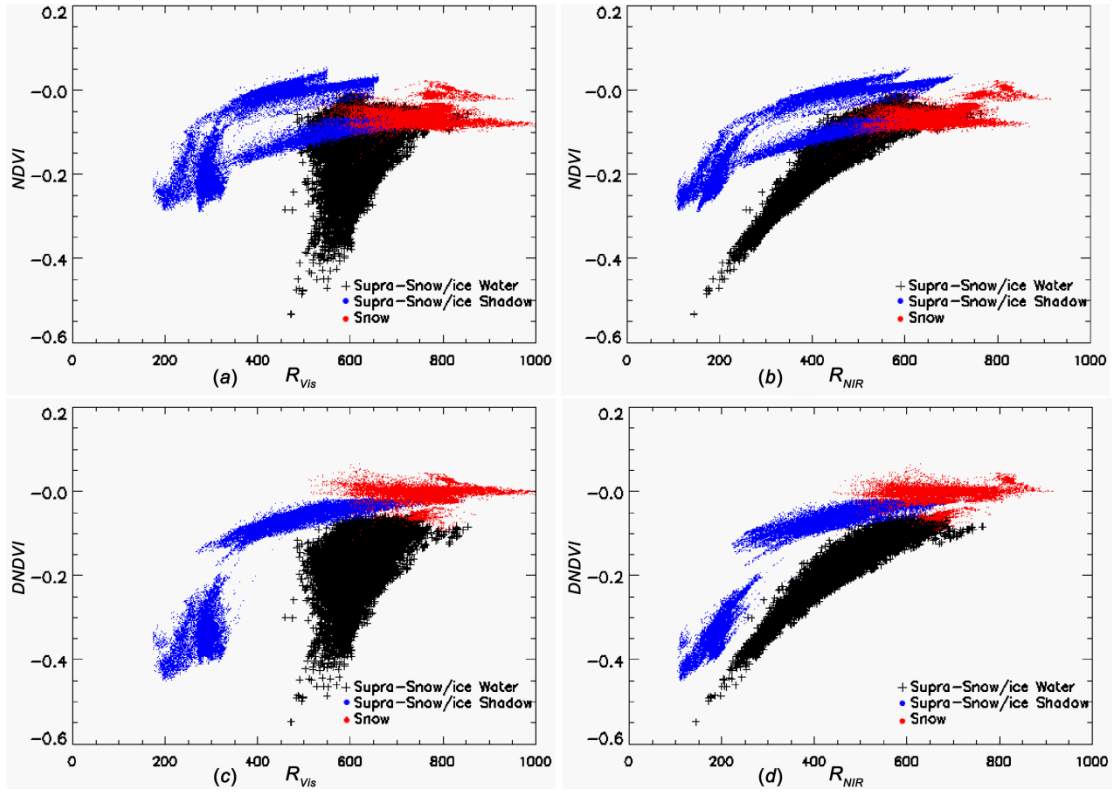
Fig. 2-11 Scatter plots of supra-snow/ice water (black), supra-snow/ice shadow (blue) and melting snow (red) surface in VIIRS imagery: (a) R_{Vis} and NDVI; (b) R_{NIR} and NDVI; (c) R_{Vis} and DNDVI; (d) R_{NIR} and DNDVI

With the four variables, threshold segmentation is used as the main method for supra-snow/ice water detection. For a snow/ice pixel, if it meets both conditions in equation (2-16), it is directly classified as a supra-snow/ice water pixel without any further processing. If a snow/ice pixel meets the conditions in equation (2-17), then it is classified as a possible supra-snow/ice water pixel and will be tested further against the DNDVI variable.

$$\begin{cases} R_{Vis} \geq 45\% \\ NDVI \leq -0.2 \end{cases} \tag{2-16}$$

$$\begin{cases} R_{Vis} \geq 40\% \\ -0.2 < NDVI \leq -0.04 \end{cases} \tag{2-17}$$

The calculation of DNDVI is a dynamic process within a moving 50×50 window. For a possible supra-snow/ice water pixel, the maximal reflectance in visible channel (R_{Vis_max}) of all snow/ice pixels (based on the snow/ice detection results) in the neighboring 50×50 window is calculated (Liang et al., 2012; Johansson and Brown, 2013). If they meet conditions (2-18), snow/ice pixels are collected and used to calculate the average NDVI of background snow/ice surface ($\overline{NDVI}$). DNDVI is calculated by subtracting $\overline{NDVI}$ from NDVI of a possible supra-snow/ice water pixel.

$$\begin{cases} R_{Vis\_max} - 10\% \leq R_{Vis} \leq R_{Vis\_max} \\ R_{Vis} \geq 55\% \\ NDVI \geq -0.05 \end{cases} \tag{2-18}$$

DNDVI is more effective in differentiating supra-snow/ice water from shadows over snow surface and melting snow surface. Based on the analysis on about 100 VIIRS granules, most shadows over snow surface with DNDVI below -0.05 have a reflectance less than 45% in visible channel, and those with reflectance larger than 45% in visible channel are mostly with DNDVI above -0.05. Melting snow surface is generally with DNDVI above -0.05. In comparison, supra-snow/ice water is with DNDVI below -0.07 and its DNDVI shows strong relationship with reflectance in near-infrared channel. Therefore, if a pixel meets condition (2-19), then it is removed from possible supra-snow/ice water pixels.

$$\text{DNDVI} > -0.06 \tag{2-19}$$

This process removes most melting snow surfaces and some shadows cast on snow surface from supra-snow/ice water pixels, and the rest shadow pixels and supra-snow/ice water pixels are further discriminated in cloud shadow removal using geometry-based method.

2.3.2.1.3 Supra-veg/bare land water detection

As the most common flood type, supra-veg/bare land floodwater detection is much more complicating than supra-snow/ice water detection due to the complex mixture of vegetation and bare land types. In mid to low latitudes, water surface is easily contaminated by sun-glint, which further complicates the situation. The detection uses a combination of methods from decision-tree approach, threshold method, histogram method to change detection with the variables: R_{Vis}, R_{NIR}, R_{SWIR}, NDVI, NDSI, NDWI and T_{ch5} based on the spectral features of water, vegetation and bare land.

The clear-sky land pixels determined by cloud and snow/ice detection are divided into two types: clear-sky land pixels with minor to moderate sun-glint contamination, and clear-sky land pixels without sun-glint contamination, by using a lookup table generated based on MERIS's sun glint flag algorithm (Montagner F, Billat V, Bélanger S, 2003). The Decision Tree (DT) approach, which is a supervised machine learning technique to support decision making by converting complex data into a relatively simple and direct viewing structure (Han, 2001), is selected as the major classification method to classify clear-sky land pixels into water, vegetation, bare land and cloud cover. For all decision tree algorithms, the process of predicting unseen instances is the same, and the differences come from the methods used to create the tree structures. The splitting criterion, stop-splitting rule, class assignment rule, and pruning method can be used in the tree generation (Quinlan, 1993). Many kinds of decision-tree algorithms have been developed based on different splitting criteria. Most notable trees include the J48graft or J48 (based on the C4.5 algorithm and was originally proposed by Quinlan (1993)), NBTree (a Naïve Bayes/Decision Tree hybrid (Kohavi, 1996)), Random Tree (RT), Random Forest (Breiman, 2001), REP Tree, BFTree, Decision Stump (DS), FT (Final Tree), and CART (Classification and Regression Trees) (Breiman et al., 1984) and so on. Although most of the tested DT algorithms have good discrimination capability, the J48graft/J48 based on the C4.5 algorithm has the best accuracy according to the test results, and thus is selected as the decision tree algorithm for supra-veg/bare land water detection. The basic strategy of the C4.5 algorithm is to select an attribute that will best separate the samples into individual classes by an 'Information Gain Ratio'. The objective is to produce the most accurate separation with the least amount of information (Han et al., 2001). The calculation of the 'Information Gain Ratio' is expressed from Equations (2-20) to (2-23).

Let S be the training set consisting of s data samples, and s (Ci) be the number records in S that belong to class Ci (i=1, 2… m) out of m classes. The information needed to classify S is:

$$Info(S) = -\sum_{i=1}^{m} \frac{s(C_i)}{s} \log_2(\frac{s(C_i)}{s})$$

(2-20)

Hence, the amount of information needed to partition S into {S1, S2…Sv} by attribute A (A has v distinct values) is:

$$Info(A \mid S) = -\sum_{j=1}^{v} \frac{S_j}{s} * Info(S_i)$$

(2-21)

And, the gain to classify S by attribute A is:

$$gain(A \mid S) = Info(S) - Info(A \mid S)$$

(2-22)

Then the 'Information Gain Ratio' is computed as:

$$gainRatio(A \mid S) = \frac{gain(A \mid S)}{Info(A \mid S)}$$

(2-23)

Based on the C4.5 algorithm, a collection of 600,000 samples from more than 500 VIIRS granules covering North America, Africa, Europe, Asia and Australia over different land cover types under different solar zenith angles is collected to train decision trees. The samples include four categories: water, bare land, vegetation and cloud cover. For water category, the samples include a wide variety of water surfaces including clean water, turbid water, wetland, water with blue-green algae, water surface with minor to moderate sun-glint contamination and so on. Because of the existence of a mixed structure for most pixels in coarse-to-moderate resolution satellite data, the spectral properties of sub-pixel areas of land can significantly affect the total reflectance of mixed water pixels. Hence, water might be detected differently over desert and forest. A well-trained tree from a desert area may fail to correctly detect water in forest areas. To reduce the uncertainty from the variance of sub-pixel land areas, a VIIRS global land cover type dataset based on global land cover from AVHRR and IGBP land cover, later updated by VIIRS surface type data in 2017, is introduced to assist the classification. For all clear-sky pixels, a J48graft tree is applied to make a preliminary classification by dividing the pixels into water, mixed water, vegetation, bare land and cloud. New samples over land cover types that have poor classification accuracy are then collected to train new decision trees. The new decision trees are utilized to do classification over specific land cover types. Altogether16 decision trees are generated for supra-veg/bare land water detection under different conditions. Fig. 2-12 shows an example of the tree structure derived from the C4.5 algorithm for the discrimination of water from bare land. The tree employs a case's attribute values to map it to a leaf, for designating one of the classes. The number in brackets following each leaf equals the number of training instances that are mapped to this leaf, and the second number after "/"in brackets (if it appears) is the number of instances that are misclassified to this leaf. A non-integral number of cases may arise. This is because when the value of an attribute in the tree is not known, DT splits the case and sends a fraction down each branch. The node in the upper level of the tree has a higher information gain ratio than in the lower level node in the classification. Therefore, as shown in Fig. 2-12, attributes/parameters like ch3, which is R_{SWIR}, and appears at the root node of the tree, is more important than those at the lower levels, such as NDSI and the reflectance in the visible channel R_{Vis} (ch1) for identifying water from bare land.
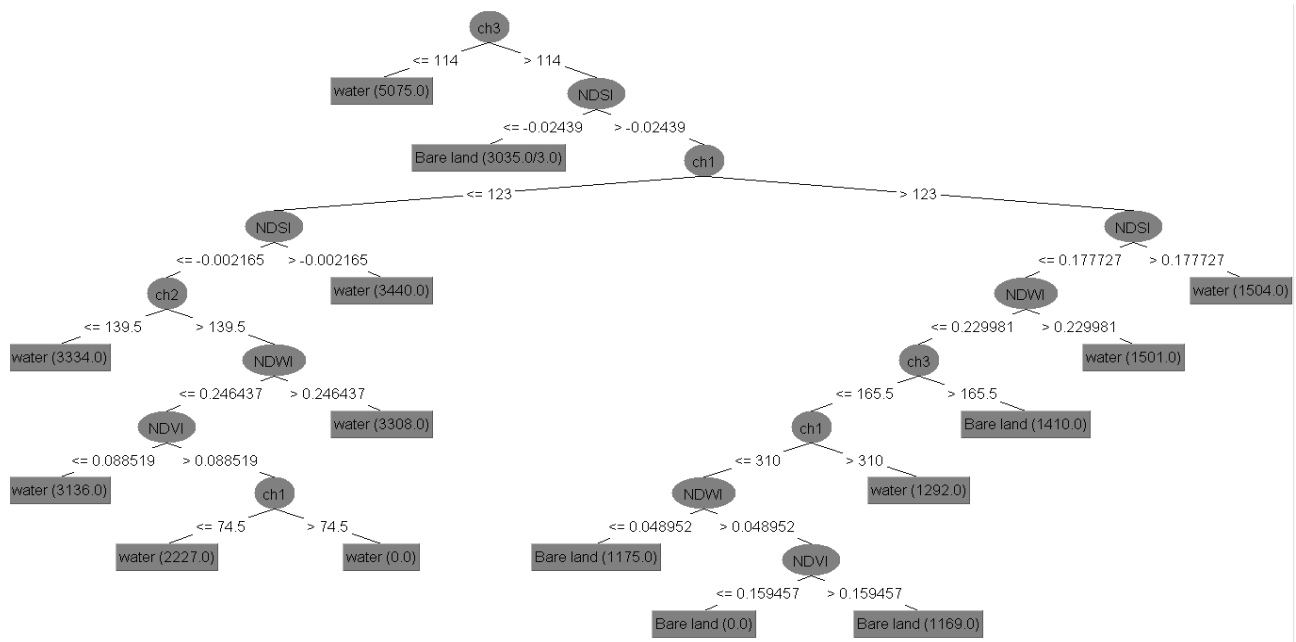
Fig. 2-12 An example of tree structure derived from the decision tree algorithm (Sun et al., 2012)

Although C4.5 algorithm shows capability to discriminate water from vegetation, bare land and thin cloud cover, the dynamic features of land surface from vegetation change, snow/ice cover, observing angles and other types such as burnt scars, urban constructions, dust storms and so on may bring uncertainty to the classification. The DT trees clusters water or water-similar pixels into water category. Some of DT-classified water pixels need to be further determined through post analysis using threshold method, histogram method and change detection, and the rest such as shadows can only be determined by shadow removal algorithms based on geometry and topography, which are described in sections 2.3.2.3 and 2.3.2.4. Some typical cases that require further confirmation through post analysis are listed as follows:

1) Dark volcanic land case: The DT classification may fail to discriminate water from dark volcanic land. In this situation, by flagging the known volcanic land in the water reference map, over these regions, if a dark volcanic land pixel is classified as water, it must meet the condition that its NDWI is above 0.25. Otherwise, it is classified as dryland. With this condition, most dark volcanic land pixels are removed from water pixels, and the rest are further removed through topography analysis during terrain shadow removal.

2) Moist vegetation land case: In highland such as Alaska, the moisture land is easily detected as water. If such a pixel is firstly detected as water, but then detected as vegetation under a DT tree for solar zenith angle larger than 40 degrees, then it is further determined with histogram method and change detection by comparing its R_{Vis}, R_{NIR}, NDVI, NDSI and T_{ch5} with the average background values in a moving 200 ×200 window. It is re-classified as water only if it meets condition (2-24):

$$\begin{cases} R_{\text{Vis}} \geq \overline{R_{Vis}} + 5\% \\ R_{\text{NIR}} \leq \overline{R_{NIR}} - 4\% \\ \quad \text{NDSI} \geq 0.2 \\ T_{\text{ch5}} \geq \overline{T_{ch5}}, \ or, \text{NDSI} \geq 0.3 \end{cases} \tag{2-24}$$

3) Water under large solar zenith angles: Under large solar zenith angles, the DT algorithm may cause more mistakes for water detection. To reduce the false detection, the classified water pixels with solar zenith angles above 45° and NDVI above 0.0, they are further confirmed by comparing the R_{NIR} and R_{SWIR} with those from background dryland. If such a pixel is with R_{NIR} 6% less than the background dryland and R_{SWIR} 5% less than the background dryland, then it is detected as water. Otherwise, it is classified as dryland.

4) Sun-glint contaminated water flag: In inland, water under sun-glint contamination is classified with DT algorithm together with water without sun-glint contamination. Some water with moderate sun-glint contamination can easily be classified as bare land because of the increased reflectance in the SWIR channel. Therefore, post analysis is done over sun-glint contaminated regions flagged by the sun-glint lookup table. If a pixel is located in minor to moderate sun-glint contamination region and is detected as water or mixed water, then if its R_{Vis} is above 10%, and R_{SWIR} is above 6%, then it is flagged as a sun-glint contaminated water pixel. If a pixel is located in minor to moderate sun-glint contamination region and is classified as bare land, it is classified as sun-glint contaminated water if it meets condition (2-25):

$$\begin{cases} R_{\text{Vis}} > 15\% \\ R_{\text{SWIR}} > 10\% \\ \text{NDSI} \geq 0.08 \\ \text{NDVI} \leq 0.05 \end{cases}, \text{or,} \begin{cases} 11\% < R_{\text{Vis}} < 18\% \\ R_{\text{SWIR}} > 9\% \\ 0.04 \leq \text{NDSI} \leq 0.08 \\ 0.05 < \text{NDVI} \leq 0.11 \end{cases} \tag{2-25}$$

5) Urban land case: Urban land with some thin snow or aerosol can be easily detected as water due to decreased reflectance in the SWIR channel but increased reflectance in the Vis and NIR channels. This is more common in Asia countries over some large urban regions with air pollution. Sensor zenith angles can affect the detection results when no atmosphere correction is done on the data. Therefore, a NDSI threshold is set under different sensor zenith angles to reduce the false detection. If an urban land pixel is classified as water by the DT algorithm, in northern hemisphere with longitude between 60°E and 180°E it must meet condition (2-26), and in other regions it must meet condition (2-27):

$$\begin{cases} NDSI \geq 10, \ when \ \theta \leq 45°, \\ NDSI \geq 15, \ when \ \theta > 45° \end{cases} \tag{2-26}$$

$$\begin{cases} NDSI \geq 2, \ when \ \theta \leq 45°, \\ NDSI \geq 4, \ when \ \theta > 45° \end{cases} \tag{2-27}$$

With the DT algorithm and post analysis, most water pixels with water fractions above 50% or so according to the statistics are successfully detected from the VIIRS imagery, although most cloud shadows, terrain shadows and some dark volcanic land are mixed in, which are removed with cloud shadow removal and terrain shadow removal algorithms.

2.3.2.2   Cloud shadow removal

All the water pixels including supra-snow/ice water and supra-veg/bare land water are applied in geometry-based cloud shadow removal algorithm to remove cloud shadow pixels from VIIRS flood maps. Based on the geometry models over ideal plane and sphere surface described in 2.3.1.2, cloud shadow positions can be predicted if cloud height is known. However, due to the uncertainty of cloud heights both in calculation and availability, the prediction may not be accurate. To reduce the

uncertainty from cloud heights, an iteration method is developed to construct the one-to-one relationship between cloud and cloud shadow using a group of adjacent cloud and cloud shadow pixels (Li et al., 2013). The one-to-one relationship is constructed based on two assumptions: 1) ignoring cloud thickness (height between cloud base and cloud top), one cloud pixel has at most one cloud-shadow pixel on the ground or over another piece of lower cloud; 2) a small portion of a cloud has similar height at each point. Thus, cloud height can be initially estimated using cloud top temperatures and nearby clear-sky land surface temperatures under average atmosphere temperature profiles, and then iterated until the one-to-one relationship is established between cloud pixels and cloud shadow pixels. If the estimated cloud height is lower or higher than the cloud's actual height, then some shadow points might not have corresponding cloud points, and some cloud points might fail to locate their corresponding shadow points. **Fig. 2-13** presents the simple concept of this method on the one-to-one relationship with the right cloud heights. In **Fig. 2-13**, three neighboring cloud points A, B and C have a height h. Points A, B and C cast their shadows at Points S_A, S_B and S_C (**Fig. 2-13** Left). When the cloud height is estimated to be Δh less than the actual height (**Fig. 2-13** Middle), cloud-shadow positions of A and B are searched in points S_B and S_C, leaving shadow point S_A without a corresponding cloud point; thus, cloud point C has no shadow. When the cloud height is estimated to be Δh higher than the actual height (**Fig. 2-13** Right), cloud-shadow points of B and C are searched in points S_A and S_B, leaving cloud point A with no shadow and shadow point S_C without cloud. Only when cloud height is estimated accurately can this one-to-one relationship be established for a group of neighboring cloud or cloud-shadow pixels.
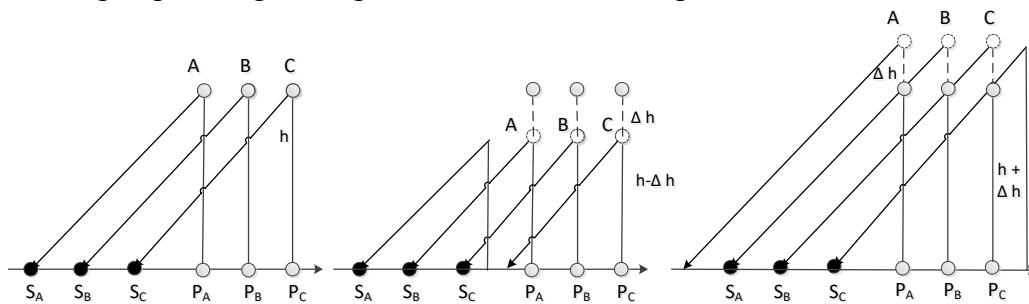
Fig. 2-13 Cloud and cloud shadow inter-determination with multiple points Left: normal cloud height; Middle: lower cloud height; Right: higher cloud height

With this method, cloud shadow pixels are determined by estimating cloud heights until the chosen shadow pixels correspond to cloud pixels. For a presumptive cloud shadow pixel, the cloud height is estimated from 0.5 km to 14 km until a cloud pixel is found using the geometric models. The brightness temperature of this cloud pixel is subsequently used to calculate a more accurate cloud height using atmosphere profile. Because the cloud height is an approximation, a new cloud-height iteration with 2 km above and below the current cloud height is performed. In this new cloud-height iteration, the found cloud pixel is used to predict a cloud-shadow pixel with the geometric relationship. If a shadow pixel is located, then the cloud height is applied to the nearby cloud and cloud-shadow pixels to test their one-to-one relationship. If all of the cloud and cloud-shadow pixels in the cloud-height iteration have corresponding cloud-shadow and cloud pixels, respectively, then the cloud height is estimated correctly. Thus, all the presumed cloud-shadow pixels determined by the cloud-height iteration are flagged as cloud shadows, and the cloud-height iteration terminates.

Alternatively, if this one-to-one relationship is not established before the iteration is terminated, then the presumptive cloud-shadow pixel is flagged as water. In this manner, most of the cloud shadows are removed from water pixels. Fig. 2-14 presents a cloud shadow removal example from VIIRS imagery. If without cloud shadow removal, most cloud shadows shown in the VIIRS false-color image (Fig. 2-14 (a)) were misclassified as flooding waters (Fig. 2-14 (b)). After applying the cloud shadow algorithm, these cloud shadows were accurately identified and removed from the VIIRS flood map (Fig. 2-14 (c)).
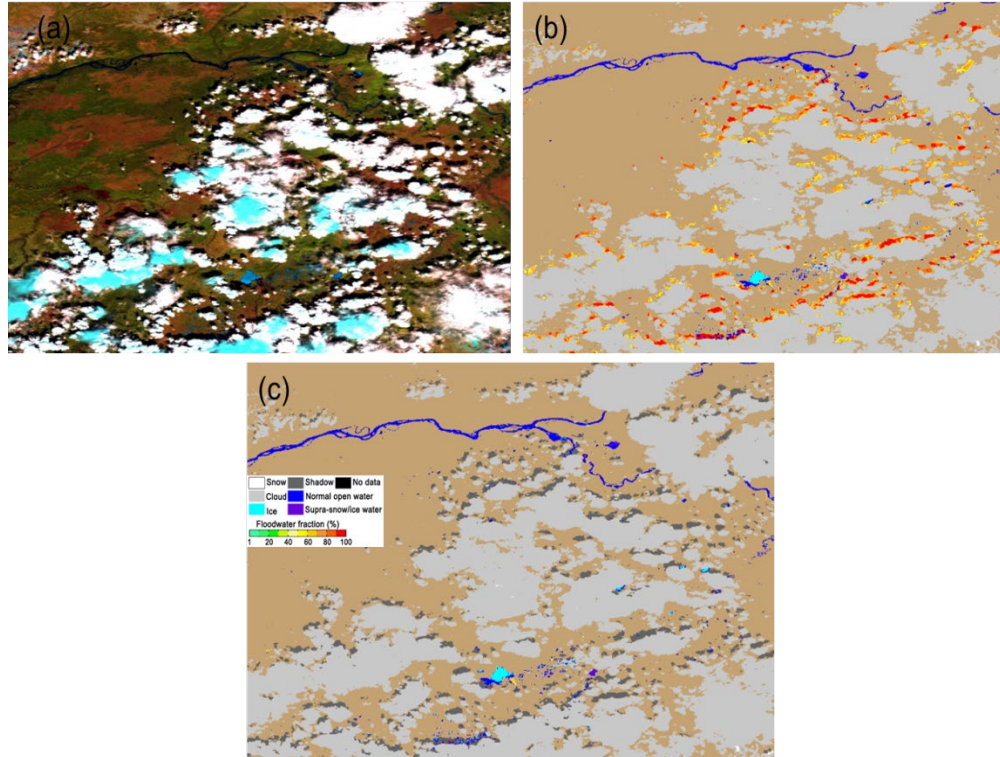
Fig. 2-14. (a) VIIRS false-color image, (b) VIIRS flood map without cloud shadow removal, and (c) VIIRS flood map after cloud shadow removal, on May 30, 2013 at 22:48 (UTC)

2.3.2.3   Terrain shadow removal

Terrain shadow removal is done after cloud shadow removal based on the surface roughness analysis described in section 2.3.1.3. Because γ, D_{mean} and D_{n} are all calculated based on a group of pixels, water pixels are clustering in groups with a neighboring search method, and the clustered water pixels are called a water object or a water polygon.

If a water object meets condition (2-28), then this object is flagged as a terrain shadow:

$$\gamma \geq 60, \text{ or,} \begin{cases} \gamma_{\text{th}} \leq \gamma < 60 \\ D_{\text{ave}} \geq D_{\text{ave\_th}} \\ |D_n| \geq 3 \\ N_{\text{w}} \leq 1 \end{cases}, \text{ or,} \begin{cases} \gamma_{\text{th}} + 5 \leq \gamma < 60 \\ D_{\text{ave}} \geq D_{\text{ave\_th}} + 20 \\ |D_{\text{n}}| \geq 3 \\ P_{\text{w}} \leq 5\%, and \, N_{\text{w}} > 1 \end{cases} \tag{2-28}$$

Where, N_{w} is the total normal water pixels calculated from the water reference map, P_{w} is the the percentage of normal water pixels in a water object, γ_{th} represents the dynamic threshold of γ,

$D_{\text{mean\_th}}$ is the dynamic threshold of D_{mean}, and $D_{\text{n\_th}}$ is the dynamic threshold of D_{n}. γ_{th}, $D_{\text{mean\_th}}$ and $D_{\text{n\_th}}$ are related to the total water/shadow pixels (N), and the total length in the horizontal ($\text{d}x$) and vertical ($\text{d}y$) directions of an object.

The derivation of $\gamma_{\text{th}}(\text{d}x, \text{d}y, N)$, $D_{\text{mean\_th}}(\text{d}x, \text{d}y, N)$ and $D_{\text{n\_th}}$ is quite empirical based on a lot of tests using VIIRS data over wide areas under different solar zenith angles. Based on the statistics on more than 10,000 VIIRS granules over North America, South America, Asia, Europe, Africa and Oceania year around, $D_{\text{n\_th}}$ is set as -3, and the other two are determined as follows based on N, N_{w}, $\text{d}x$ and $\text{d}y$:

If $N < 25$, γ_{th} is set as 15, $D_{\text{ave\_th}}$ is 35.

If $N \geq 25$, γ_{th} and $D_{\text{mean\_th}}$ are calculated using Equations (2-29) and (2-30):

$$\gamma_{\text{th}} = 0.12 \times \max(\text{d}x, \text{d}y) + 18 \qquad (2\text{-}29)$$
$$D_{\text{mean\_th}} = 0.2 \times \max(\text{d}x, \text{d}y) + 50 \qquad (2\text{-}30)$$

Even if γ, D_{mean} and D_{n} meet the thresholds, some real floodwater objects may be removed as terrain shadows. To maximally avoid this situation, N_{w} and the percentage of normal water pixels (P_{w}) are used along with γ, D_{mean} and D_{n}. This is because most floodwater happens around normal water bodies such as rivers, lakes or reservoirs and hence if an object is a real floodwater, there should be some normal water pixels within the object. If an object is without any normal water pixels, then the object is taken as terrain shadows as long as γ, D_{mean} and D_{n} meet the defined thresholds. If N_{w} is larger than 1, but the percentage of normal water pixels (P_{w}) is less than 5%, the object is to be determined under an increasing thresholds than calculated ones from Equation (2-29) and (2-30). For VIIRS imagery, $\gamma_{\text{th}} + 5$ and $D_{\text{mean\_th}} + 20$ are utilized for removal in this situation.

With the method, more than 95% terrain shadows can be removed from VIIRS flood maps. Additionally, the method also helps remove some other false water detection such as some residual cloud shadows, dark volcanic land and burn scars (Li et al., 2015). Fig. 2-15 demonstrates an example on terrain shadow removal with this method. If without applying the terrain shade removal algorithm, most terrain shadows along the mountains in the VIIRS false-color image (Fig. 2-15 (a)) were misclassified as flooding water (Fig. 2-15(b)). After applying the method, these terrain shadows were successfully identified and are removed from the VIIRS flood map (Fig. 2-15(c)).
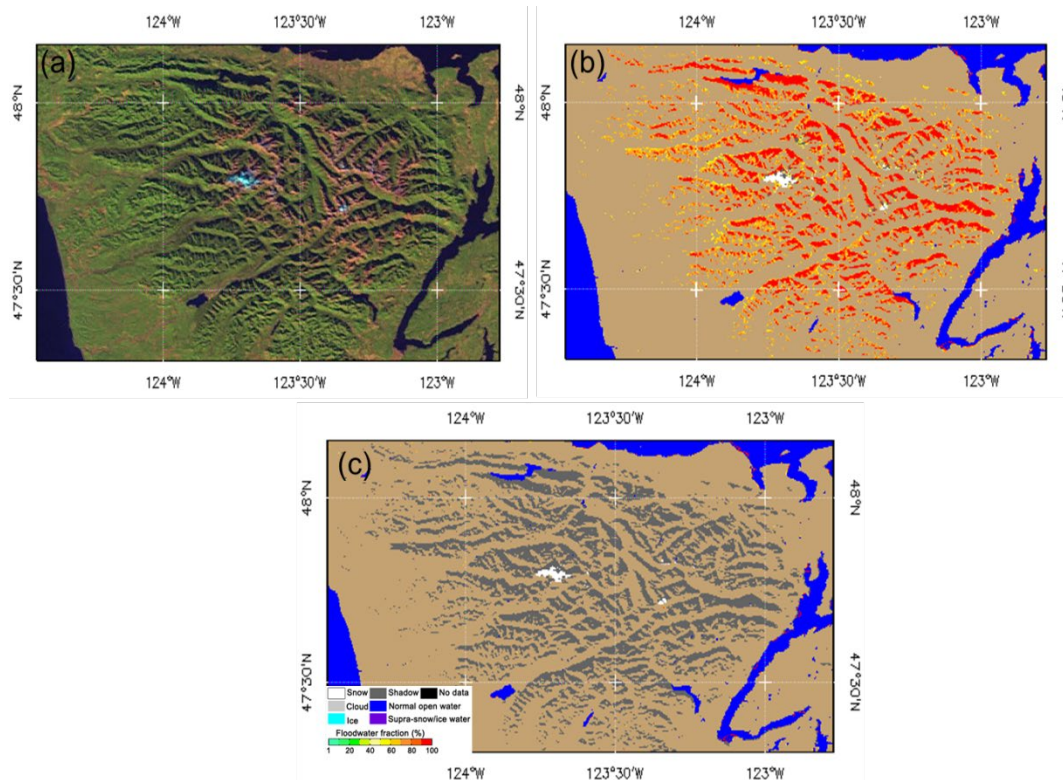
Fig. 2-15 (a) VIIRS false-color image, (b) VIIRS flood map without terrain shade removal (b), and (c) VIIRS flood map after terrain shadow removal, on Nov. 15, 2014 at 21:02 (UTC).

2.3.2.4   Water fraction retrieval

As described in section 2.3.1.4, the VFM retrieves water fractions for supra-veg/bare land floodwater. For supra-veg/bare land water without sun-glint contamination, a dynamic nearest neighboring searching method is used by considering the mixture structure of sub-pixel land portion, and for supra-veg/bare land water with minor to moderate sun-glint contamination, histogram method is applied.

2.3.2.4.1   Dynamic Nearest Neighboring Searching (DNNS) method

As shown in Fig. 2-3, the reflectance of clean water in the SWIR channel is close to 0. Although the reflectance may increase slightly with suspending matter, compared to vegetation and bare land, the reflectance of water in this channel can still be ignored (K. Kallio, 1999; Giordano, 2000; Balkanov, 2003). Therefore, the reflectance of a mixed water pixel in this channel is mainly from land with a total fraction of $(1 - f_w)$. For a mixed water pixel, the reflectance in the Vis, NIR and SWIR channels can be expressed from Equations (2-31) to (2-33).

$$R_{Vis} = (1 - f_w) * R_{Vis\_land} + f_w * R_{Vis\_water} \qquad (2\text{-}31)$$
$$R_{NIR} = (1 - f_w) * R_{NIR\_land} + f_w * R_{NIR\_water} \qquad (2\text{-}32)$$
$$R_{SWIR} = (1 - f_w) * R_{SWIR\_land} \qquad (2\text{-}33)$$

With equations (2-31) to (2-33), because the reflectivity of a surface type is fixed under the same observing conditions, then the ratios $\frac{R_{Vis}}{R_{SWIR}}$ and $\frac{R_{NIR}}{R_{SWIR}}$, which are mainly affected by the percentages of surface types, can reflect the mixture structure of land types.

Based on Equations (2-31) to (2-33), the ratios $\frac{R_{Vis}}{R_{SWIR}}$ and $\frac{R_{NIR}}{R_{SWIR}}$ of a mixed water pixel can be written as:

$$\frac{R_{Vis\_mix}}{R_{SWIR\_mix}} \approx \frac{R_{Vis\_land}}{R_{SWIR\_land}} + f_w \frac{R_{Vis\_water}}{R_{SWIR\_mix}} \tag{2-34}$$

$$\frac{R_{NIR\_mix}}{R_{SWIR\_mix}} \approx \frac{R_{NIR\_land}}{R_{SWIR\_land}} + f_w \frac{R_{NIR\_water}}{R_{SWIR\_mix}} \tag{2-35}$$

By transmutation, Equations (2-34) and (2-35) can be written as:

$$\frac{R_{Vis\_land}}{R_{SWIR\_land}} \approx \frac{R_{Vis\_mix}}{R_{SWIR\_mix}} - f_w \frac{R_{Vis\_water}}{R_{SWIR\_mix}} \tag{2-36}$$

$$\frac{R_{NIR\_land}}{R_{SWIR\_land}} \approx \frac{R_{NIR\_mix}}{R_{SWIR\_mix}} - f_w \frac{R_{NIR\_water}}{R_{SWIR\_mix}} \tag{2-37}$$

For a mixed water pixel f_w has a range from 0.0 to 1.0, and thus the ranges of the ratios $\frac{R_{Vis}}{R_{SWIR}}$ and $\frac{R_{NIR}}{R_{SWIR}}$ have the following relationships:

$$\frac{R_{Vis\_mix}}{R_{SWIR\_mix}} - \frac{R_{Vis\_water}}{R_{SWIR\_mix}} < \frac{R_{Vis\_land}}{R_{SWIR\_land}} < \frac{R_{Vis\_mix}}{R_{SWIR\_mix}} \tag{2-38}$$

$$\frac{R_{NIR\_mix}}{R_{SWIR\_mix}} - \frac{R_{NIR\_water}}{R_{SWIR\_mix}} < \frac{R_{NIR\_land}}{R_{SWIR\_land}} < \frac{R_{NIR\_mix}}{R_{SWIR\_mix}} \tag{2-39}$$

The relationships described in Equations (2-38) and (2-39) provide the range to search for the nearby pure land pixels that are with similar mixture structure of land types to the sub-pixel land portion. For VIIRS water fraction retrieval, because R_{Vis} does not show significant difference over vegetation, bare land and water, and most water pixels with water fractions less than 50% are not detected by the DT algorithm, Equation (2-38) tends to cluster many undetected minor water pixels as the pure land pixels, which might result in under-estimated R_{ch_land}. Therefore, only Equation (2-39) is applied to search for nearest neighboring dryland pixels. Because R_{SWIR} varies little with water types in comparison to R_{Vis} and R_{NIR}, the SWIR channel is used as the major channel for water fraction retrieval over supra-veg/bare land water without sun-glint contamination.

For mixed pixels with large water fractions (for example, f_w is larger than 0.9), the radiance from the sub-pixel land portion in channel 6 is close to the sub-pixel water portion because of the small fraction of land. In this case, the reflectance of the water portion in this channel cannot be ignored and equation (2-39) may not be applicable or fail to search any effective dryland pixels nearby because of larger ratio values of $\frac{R_{NIR}}{R_{SWIR}}$. However, since the total reflectance of a mixed water pixel in SWIR channel is also very low and close to a pure water pixel, the mixture structure of land types in the sub-pixel land portion does not show any significant impact on the total reflectance,

which means any pure land pixel nearby can be used. Therefore, the average reflectance of nearby pure land pixels in channel 6 can be used as R_{ch_land} for water fraction calculation from Equation (2-15).

Although most pure water pixels can be defined from water reference map, many floodwater pixels are also with f_w close to 1.0 and these pure floodwater pixels help derive more accurate R_{ch_water} for water fraction retrieval nearby than pure water pixels from lakes or ocean surface nearby in the water reference map. Generally, pure water pixels are with typical water spectral features and can be directly confirmed using NDVI and R_{SWIR}. For VFM, if a water pixel meets the condition (2-40), it is defined as a pure water pixel:

$$\begin{cases} \text{NDVI} < -0.15 \\ R_{SWIR} \leq 6\% \\ R_{Vis} \leq 30\% \end{cases}, \text{or,} \begin{cases} \text{NDVI} < -0.1 \\ R_{SWIR} \leq 5\% \\ R_{Vis} \leq 30\% \end{cases}, \text{or,} \begin{cases} \text{NDVI} < -0.05 \\ R_{SWIR} \leq 2\% \\ R_{Vis} \leq 30\% \end{cases} \quad (2\text{-}40)$$

Therefore, for the water fraction retrieval with the DNNS method, pure water pixels are firstly defined with condition (2-40), and for the rest mixed water pixels, clear-sky land pixels that satisfy Equation (2-39) are searched in a moving window from 25 to 100, depending on how many qualified pure land pixels are searched in the current window. The average or median reflectance of all searched land pixels is taken as R_{ch_land}. If no land pixels are searched, then the average or median reflectance of all land pixels nearby is taken as R_{ch_land}. The nearest pure water pixels are also aggregated to calculate the average or median channel reflectance as the reflectance of pure water R_{ch_water}. With R_{ch_land} and R_{ch_water}, water fraction f_w is calculated with Equation (2-15).

2.3.2.4.2 Histogram method

Different to supra-veg/bare land water without sun-glint contamination, water with minor to moderate sun-glint contamination shows quite different spectral features. One important feature is that R_{SWIR} increases rapidly with sun-glint and the reflectance of water surface in this channel is not close to 0 anymore and thus cannot be ignored. Therefore, the DNNS method cannot be used for water retrieval in this situation. With more radiance from the sub-pixel water portion, the proportion of radiance from sub-pixel land portion decreases substantially, and the impact from mixture structure of land types in the sub-pixel land portion is relatively small and thus may be ignored. Therefore, the histogram method is used for water fraction retrieval in this situation (Sheng et al., 2001).

For a confirmed water pixel with sun-glint contamination, the average or median reflectance of all land pixels in the neighboring 100×100 moving window is taken as R_{ch_land}. The average or median reflectance of all pure water pixels with sun-glint contamination in the neighboring moving window from 100 to 400 is taken as R_{ch_water}, depending on the number of searched pure water pixels with sun-glint contamination in the current window. If no pure water pixels with sun-glint contamination are searched, then R_{ch_water} is calculated from all the pure water pixels searched in the neighboring moving windows sizing from 100 to 400.

With R_{ch_land} and R_{ch_water}, water fraction f_w is calculated with Equation (2-15).

2.3.2.5   Change detection for minor water extraction

As mentioned in section 2.3.2.1, the DT algorithm only successfully detects water pixels with water fractions above 50% or so. To detect floodwater pixels with water fractions less than 50%,

change detection is used as the main approach around the confirmed water pixels and existing rivers, lakes, and reservoirs in the ancillary water reference map. The method determines a minor water pixel by either comparing water signals before and after flooding, or comparing water signals with surrounding confirmed clear-sky land pixels that have similar land cover types to the minor water pixel. To reduce the dependence on historic data, the VFM chooses to compare the spectral variables R_{Vis}. R_{NIR}, R_{SWIR}, NDSI and T_{ch5} of a minor water pixel with those from the surrounding clear-sky land.

For a confirmed water pixel, average reflectance in Vis, NIR and SWIR channels are calculated in the neighboring 50×50 window on vegetation ($\overline{R_{Vis\_V}}, \overline{R_{NIR\_V}}, \overline{R_{SWIR\_V}}, \overline{NDSI_V}$) and bare land ($\overline{R_{Vis\_B}}, \overline{R_{NIR\_B}}, \overline{R_{SWIR\_B}}, \overline{NDSI_B}$) with the same land cover types, respectively. The variable difference between the minor water pixel and the surrounding land pixels are referred as $DR_{Vis}, DR_{NIR}, DR_{SWIR}$, and $DNDSI$, respectively. All the land pixels around a confirmed water pixel, which are within 30m elevation difference to the confirmed water pixel, are applied in reflectance comparison to the background. For a vegetation pixel, if it meets condition (2-41), then it is determined as a minor water pixel, and for a bare land pixel, if it meets condition (2-42), then it is determined as a minor water pixel.

$$\begin{cases} R_{\text{NIR}} \leq 35\% \\ R_{\text{SWIR}} \leq 20\% \\ NDSI \geq \overline{NDSI_V} \\ DR_{NIR} \leq DR_{NIR\_th} \\ DR_{SWIR} \geq DR_{SWIR\_th} \\ DNDSI > DNDSI_{th} \\ DR_{Vis} \geq DR_{Vis\_th} \end{cases} \tag{2-41}$$

$$\begin{cases} R_{\text{Vis}} < 25\% \\ R_{\text{NIR}} < 25\% \\ R_{\text{SWIR}} < 25\% \\ NDSI \geq \overline{NDSI_B} \\ DR_{NIR} \leq DR_{NIR\_th} \\ DR_{SWIR} \geq DR_{SWIR\_th} \\ DNDSI > DNDSI_{th} \\ R_{Vis} \geq \overline{R_{Vis\_V}} \end{cases} \tag{2-42}$$

In conditions (2-41) and (2-42), $DR_{Vis\_th}, DR_{NIR\_th}, DR_{SWIR\_th}$ and $DNDSI_{th}$ are thresholds that defined in vegetation and bare land with different land cover types. For vegetation pixels over forest, $DR_{NIR\_th}, DR_{SWIR\_th}$ and $DNDSI_{th}$ are set as -8%, -5% and -0.35, in urban land, they are set as -12%, -11% and -0.1, and in other land cover types, they are set -9%, -6% and -0.3. For bare land pixels over desert, $DR_{Vis\_th}, DR_{NIR\_th}, DR_{SWIR\_th}$ and $DNDSI_{th}$ are set as -8%, -12%, -15% and -0.3, in urban land, they are set as -7%, -10%, -11% and -0.15, in grassland and open shrub land, they are set as -6.5%, -10%, -11% and -0.25, in cropland and close shrub land, they are set as -6%, -9%, -10% and -0.2, and in other land cover types, they are set -6%, -9%, -10.5% and -0.25.

The change detection successfully detects many water pixels with water fractions less than 50% in the VIIRS flood maps, although it fails to pick up water pixel with water fractions below 20% or so. Some cloud shadows and terrain shadows are also counted in. Therefore, the detected minor

water pixels are required removing cloud shadows and terrain shadows using the methods described in sections 2.3.2.2 and 2.3.2.3, as well as water fraction retrieval described in section 2.3.2.4.

2.3.2.6   Flood water determination

The supra-snow/ice water is kept as an independent type in the VIIRS flood maps to differentiate from supra-veg/bare land water. Therefore, only the retrieved supra-veg/bare soil water fractions are compared against the water reference map. The water reference map used in VFM is a combination of the 2015's MODIS 250-m global water mask, the water layer in the 30-m National Land Cover Dataset (in the USA) and the global 150-m water mask from ESA's Climate Change Initiative (CCI). The MODIS 250-m global water mask is resampled to 375-m water/no water mask, and the 30-m National Land Cover Dataset in the CONUS and the 150-m CCI water mask are resampled to 375-m water mask by calculating water fractions at 375-m grids. For a detected water pixel from the VIIRS imagery, if it is in the water reference map with less than 1% water fraction or shown as no water (it is a land pixel in the water reference map), then the pixel is determined as floodwater directly and represented with the retrieved water fraction. If in the water reference map it is with water fraction larger than 1% or shown as water, then the pixel is only determined as floodwater when the retrieved water fraction is at least 40% larger than that in the water reference map. Otherwise, it is determined as a normal water pixel. Therefore, in VIIRS flood maps, supra-veg/bare soil floodwater pixels are represented in fractions from 1% to 100%, which provides end users with more detail on flood extent.

2.3.2.7   Maximal water fraction composition

With the near real-time (NRT) VIIRS flood maps, a maximal water-fraction composition process can help filter out cloud cover to derive the maximal flood event during a period. In a composited flood map, a pixel is assigned as a flooding pixel as long as it is detected as a flooding pixel in any NRT flood maps during that period, and the maximal floodwater fraction among all the NRT flood maps is used as its composited water fraction. The VFM also composites snow/ice cover and clear-sky land to derive the maximal snow/ice cover and clear-sky land in the final composited flood maps. If a pixel is not detected as flood but is detected as snow/ice cover in any NRT flood maps, then it is assigned as a snow ice pixel. Otherwise, if it is not detected as floodwater or snow/ice cover, but is detected as a dryland pixel in any NRT flood maps, then it is detected as a dryland pixel in the composited flood map. If it is detected as cloud cover in all the NRT flood maps, then it is assigned as a cloud pixel in the composited flood map. In this way, the composited flood map shows the maximal clear-sky coverage with the maximal floodwater fractions during a period. The routinely generated composited VIIRS flood maps include daily composition and 5-day composition from Suomi-NPP and NOAA-20. Fig. 2-16 demonstrates the flow chart of the composition process.
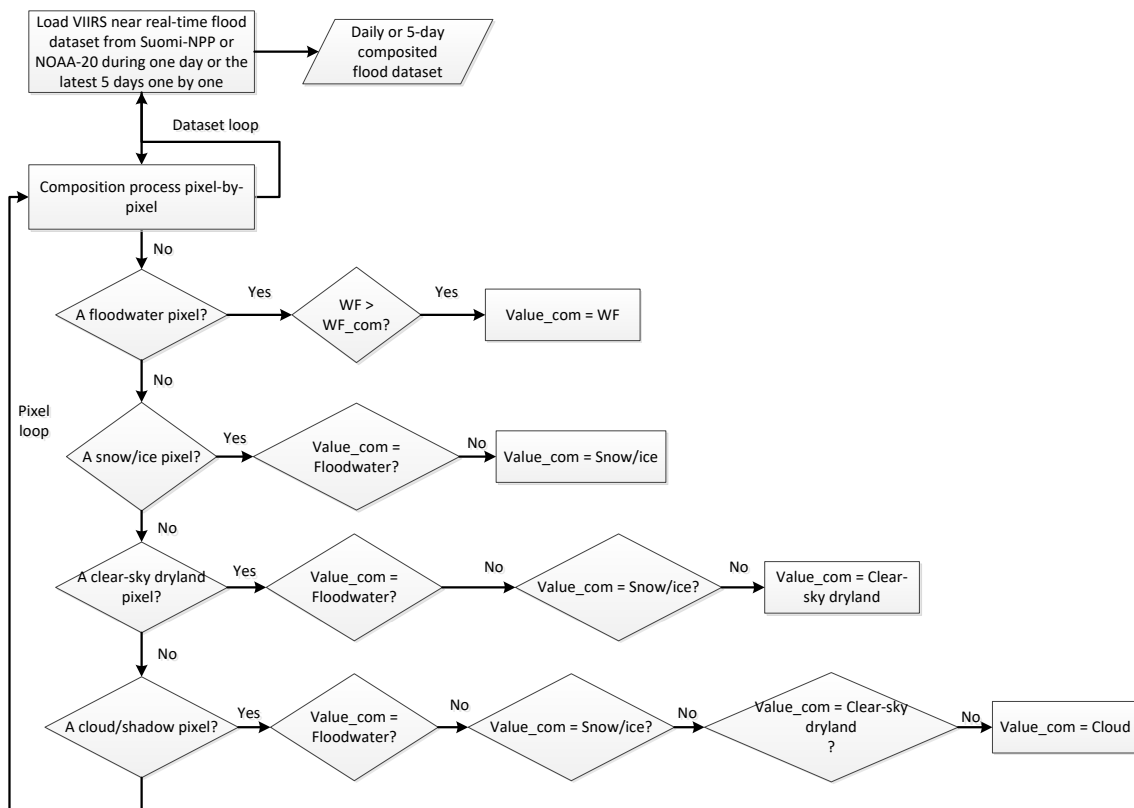
Fig. 2-16 Flow chart of the VFM composition process

2.4 Algorithm Output

The algorithm outputs include:

- VIIRS NRT floodwater detection dataset in 89-S granules
- Quality flag of the VIIRS NRT floodwater detection dataset
- VIIRS NRT floodwater detection dataset in the eight NWS domains
- Quality flag of the VIIRS NRT floodwater detection dataset in the eight NWS domains
- VIIRS daily composited floodwater dataset
- Quality flag of the VIIRS daily composited floodwater dataset
- VIIRS 5-day composited floodwater dataset
- Quality flag of the VIIRS 5-day composited floodwater dataset

The VIIRS NRT floodwater detection dataset and its quality flag are with the same size of gridded VIIRS NRT granules, or in NWS 8 defined domains (Fig. 2-17). The daily and 5-day composites and the corresponding quality flags are in 136 defined areas of interest (AOI) covering global land between 60°S and 75°N in latitudes (Fig. 2-18). The formats include netCDF, geotiff and shapefile. Ultimately, there are eight pixel types in the final VIIRS flood maps: cloud, snow cover, river/lake ice cover, shadows (including cloud shadows and terrain shadows), clear-sky land (including vegetation and bare soil), normal open water, supra-snow/ice water (including mixed water&ice and melting ice surface), and supra-veg/bare soil flooding water fractions. Table 2-4 lists the definition of the VIIRS output floodwater dataset, and the quality flags are shown in Table 2-5. Fig. 2-19, Fig. 2-20, and Fig. 2-21

present an example of VIIRS NRT flood maps in granule and in NWS domains, a daily composited flood map, and a 5-day composited flood map, respectively.

Table 2-4 Definition of types of WaterDetection dataset in the output VFM netCDF file

Value	Definition
1	Fill value: bad data, solar eclipse, data with solar zenith angles out of processing range
15	Open water without water fraction retrieval
16	Clear-sky bare land
17	Clear-sky vegetation
20	Snow cover
27	River/lake ice cover
30	Cloud cover
38	Supra-snow/ice water, mixed ice&water, or ice in melting status
50	Shadow: cloud shadow and terrain shadow
100	Open normal water: river, lake, reservoir, ocean
101~200	Water fractions of supra-vegetation bare land floodwater

Table 2-5 Definition of QualityFlag dataset in the output VFM netCDF file

Value	Definition
0	High-quality detection
1	Moderate-quality detection
2	Low-quality detection
255	Fillvalue

## Eight Domians in the USA
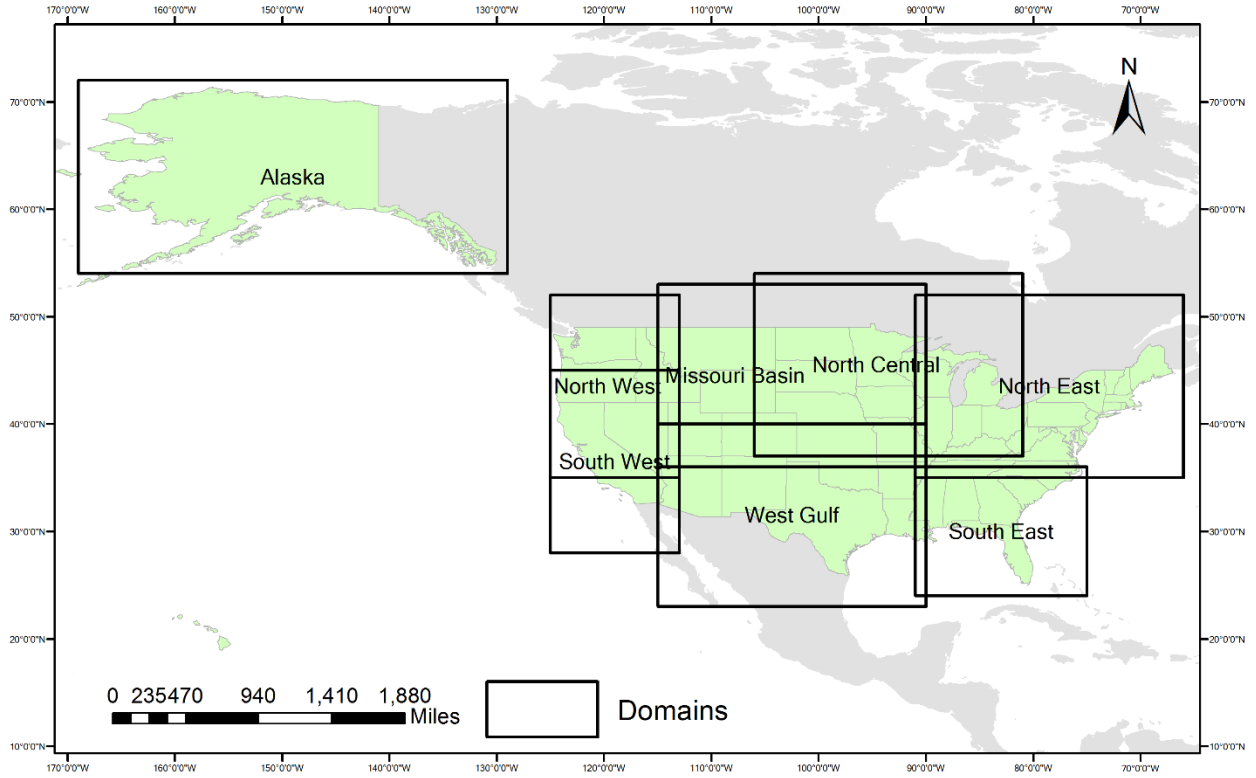
Fig. 2-17 Sketch of NWS 8 domains
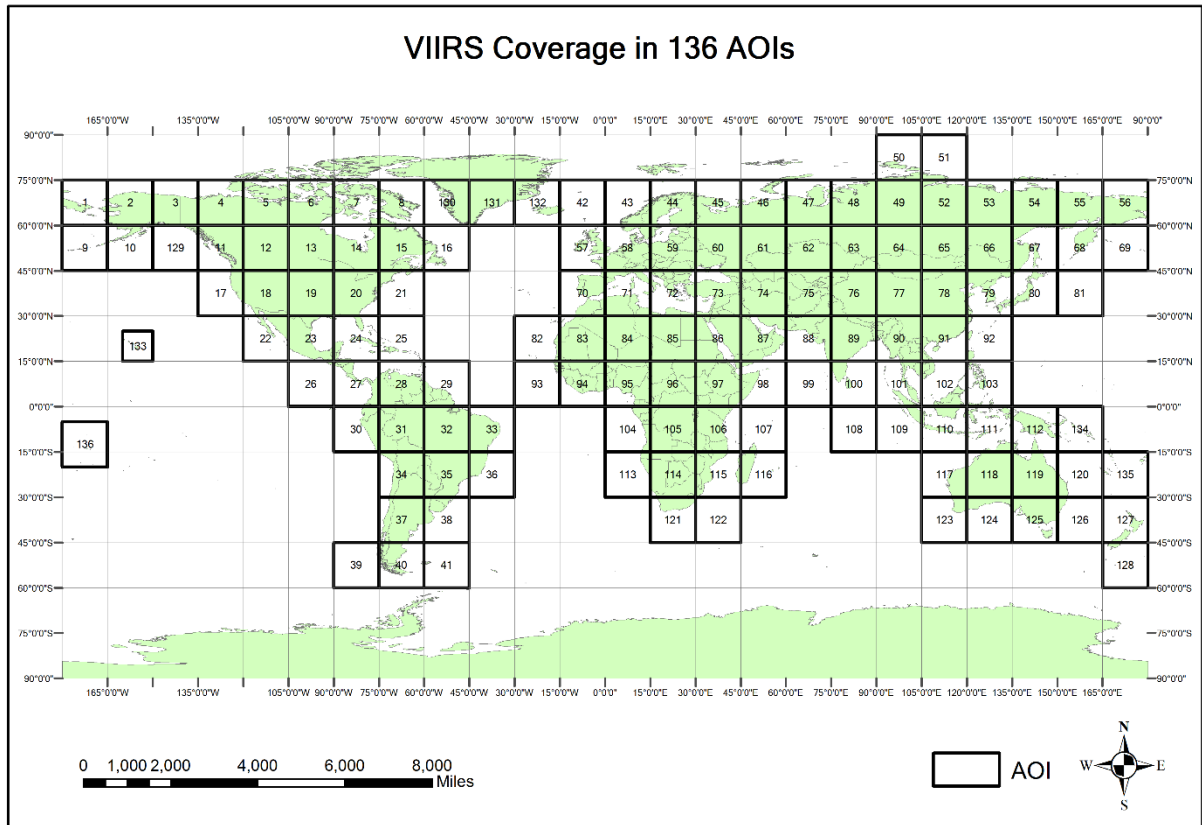
Fig. 2-18 Sketch of global 136 AOIs for VFM daily and 5-day composited products
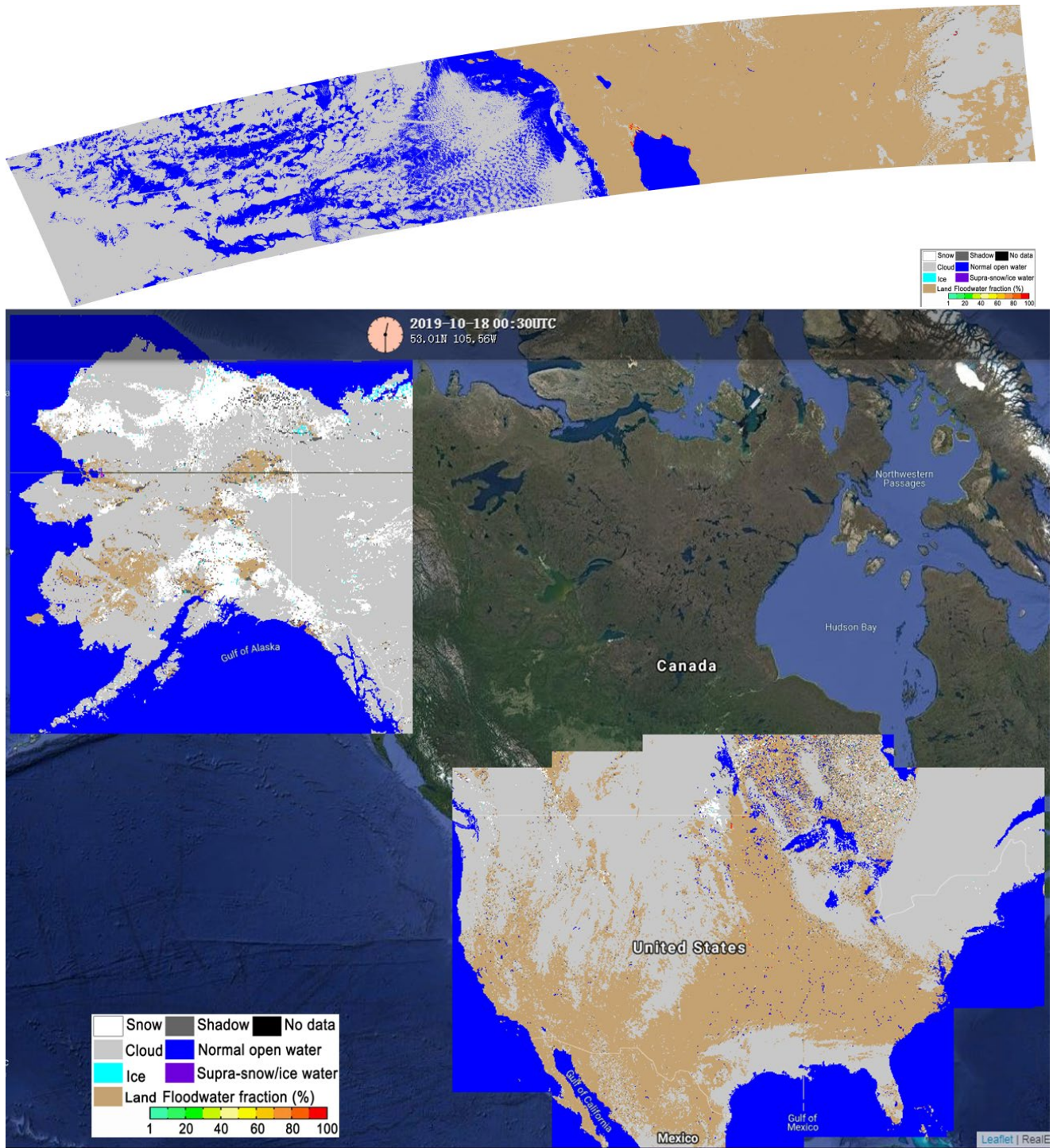
Fig. 2-19 An example of VIIRS NRT flood map in 89-S granule
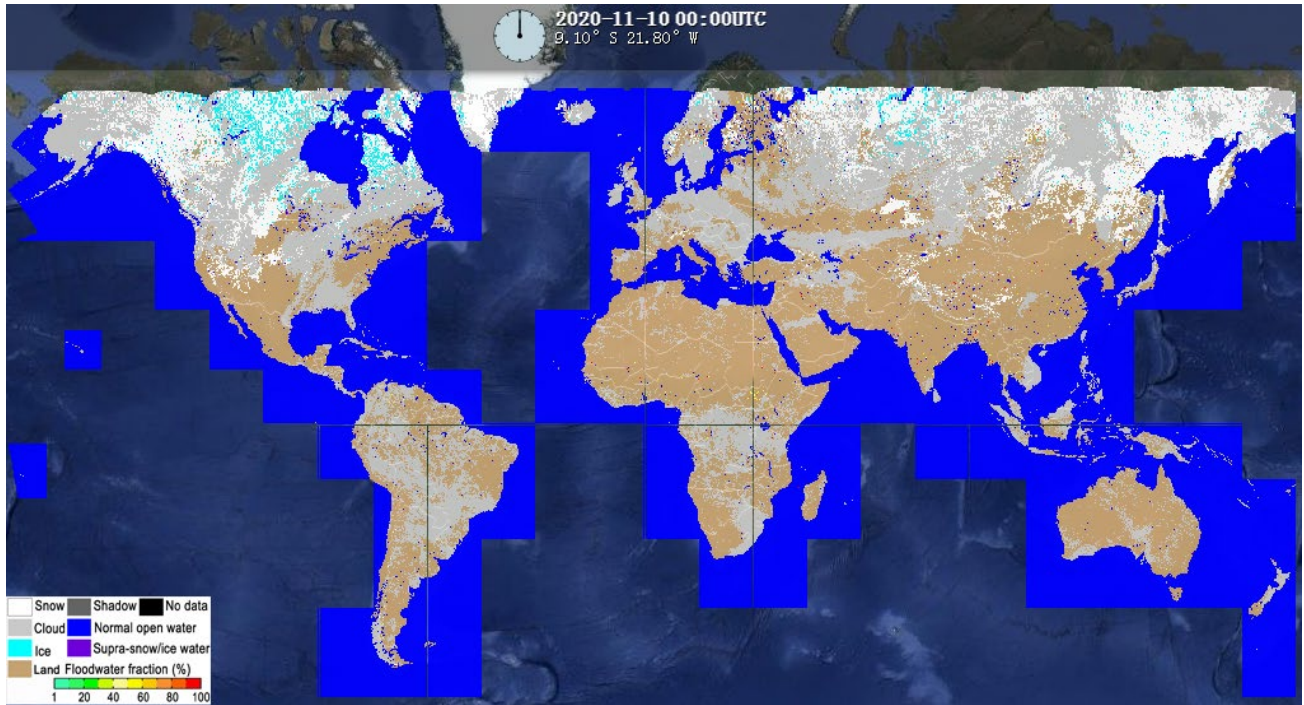
Fig. 2-20 An example of VIIRS global daily composited flood map in the 136 AOIs
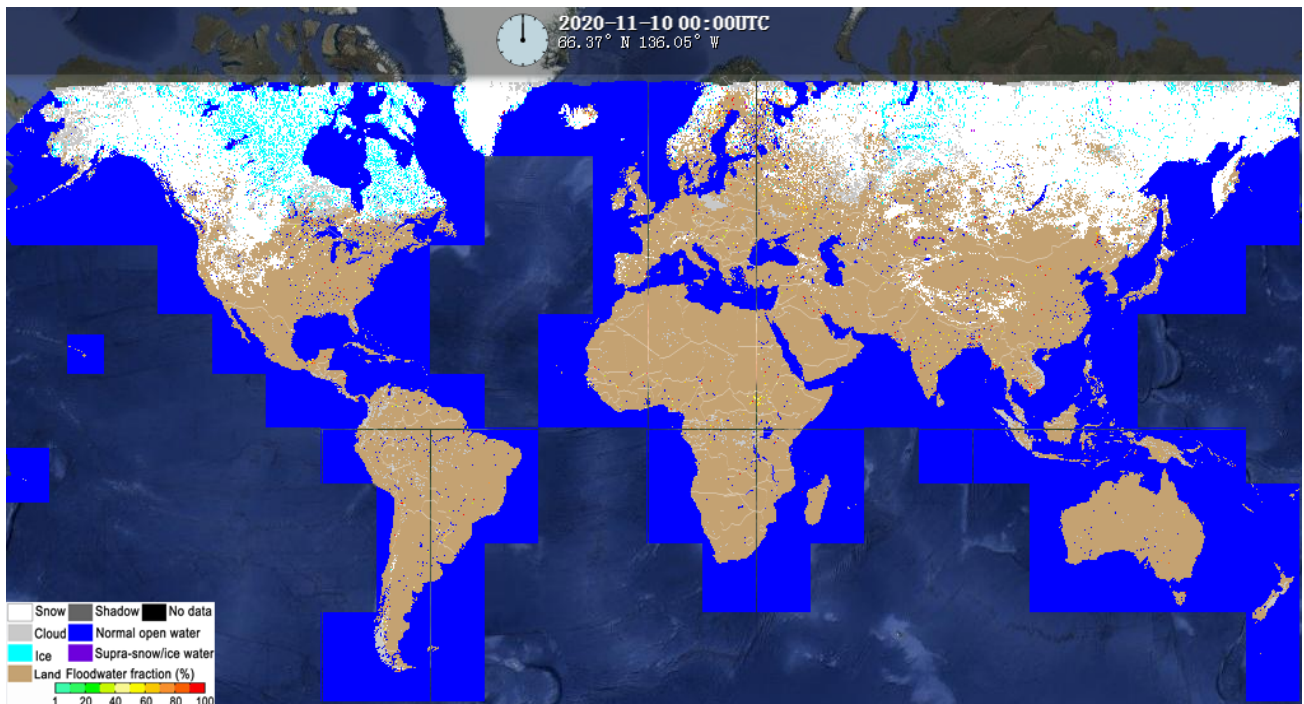
Fig. 2-21 An example of VIIRS global 5-day composited flood map in the 136 AOIs

2.5 Performance Estimates

2.5.1 Test Data Description

One VIIRS 89-S granule from NOAA-20 data is used as the test data to run the algorithm and software. The test datasets include VIIRS terrain-corrected navigation data (GITCO), VIIRS Imager band 01 (SVI01), band 02 (SVI02), band 03 (SVI03), band 05 (SVI05), and VIIRS enterprise cloud mask data (JRR-CloudMask), which are listed as following:

GITCO_j01_d20200225_t1909150_e1910395_b11768_c20200226160606186943_nobc_ops.h5
SVI01_j01_d20200225_t1909150_e1910395_b11768_c20200226160556032790_nobc_ops.h5
SVI02_j01_d20200225_t1909150_e1910395_b11768_c20200226160559483258_nobc_ops.h5
SVI03_j01_d20200225_t1909150_e1910395_b11768_c20200226160600612879_nobc_ops.h5
SVI05_j01_d20200225_t1909150_e1910395_b11768_c20200226160534051648_nobc_ops.h5
JRR-CloudMask_v2r1_j01_s202002251909150_e202002251910395_c202002251935310.nc

With the test data, VIIRS_Swath_Projection module output the gridded 89-S granules with the four Imager bands (SVI01, SVI02, SVI03 and SVI05), and solar zenith angle, solar azimuth angle, sensor zenith angle and sensor azimuth angle in 375-m spatial resolution, and the gridded JRR-CloudMask in 750-m spatial resolution:

GITCO_Prj_SVI_j01_d20200225_t1909150_e1910395_b11768_cspp_dev_000.h5
JRR-CloudMask_ j01_prj_s202002251909150_e202002251910395_000.h5

The two gridded datasets are used for VIIRS flood detection, and the VIIRS NRT floodwater dataset and quality flag are generated in netCDF format:

VIIRS-Flood_j01_s202002251909150_e202002251910395_c202003050039039.nc

The output VIIRS NRT floodwater dataset is divided into 8 NWS domains or 136 AOIs for daily and 5-day composition. More detail will be provided in "System Maintenance Manual".

2.5.2 Sensor Effects

Because the VFM uses VIIRS Imager band 01 (VIS), band02 (NIR) and band 03 (SWIR) to detect water and retrieve water fractions, sensor performance may affect the accuracy of water detection and fraction retrieval. Particularly, the SWIR channel is a key channel for water detection and fraction retrieval. The sensitivity of spectral response in this channel is quite important for the product quality. Although the VFM algorithm uses DT approach and change detection as the major approaches for water detection, which is tolerant with slight fluctuation in channel reflectance, the product quality is still affected by the stability of calibration. Because the VIIRS Imager bands are not atmospheric corrected, sensor observing geometry is another uncertainty to the detection and water fraction retrieval. Under large sensor zenith angles, due to atmosphere effect, less water pixels may be detected and water fractions may be underestimated due to larger reflectance than actual one. Although VIIRS granules are with relatively constant spatial resolution across the entire scan, on the edges of a scan, the spatial resolution is still not as good as nadir regions, and thus may decrease the quality as well. For NOAA-20, the stripes in the VIIRS I-band 03 (SWIR) may cause problems, although the stripes have been interpolated with the neighboring scans, the accuracy over these scans decreases accordingly.

2.5.3 Retrieval Errors

The VFM algorithm includes water detection and water fraction retrieval. The water fraction retrieval accuracy are directly affected by water detection errors. Currently, there are several major errors from the water detection algorithm described below.

Some cloud shadows cast by some thin clouds, which are detected as water, remain unremoved in the VIIRS flood maps due to the uncertainty of cloud detection and underestimation of cloud heights of these clouds. This is the major error source of the VFM products.

Some terrain shadows over flat topography may not be removed with the object-based terrain removal algorithm based on surface roughness analysis. Although it is quite rare, it happens mostly in high latitudes during winter season under large solar zenith angles.

The minor water detection algorithm detects water pixels with small water fractions using the information from the background dryland. Inevitably, some muddy or moist land after tides or floods may be falsely detected as water by the algorithm.

Under sun-glint contamination, water detection accuracy decreases especially over water surface with moderate sun-glint contamination, comparing to water detection without sun-glint contamination. Because sun-glint is closely related to solar angles, this kind of error mainly occurs in mid to low latitudes during summer.

The VFM algorithm detected some water with salt-like clay background. This type of water looks similar to snow/ice. In very rare situation, the algorithm may take some rainforest with some smoke as water because of the decreased reflectance in the SWIR channel.

On the granule edges between two continuous granules, floodwater may not be applied in cloud shadow removal because the clouds that cast the shadows are located in the other granule. In this situation, the VFM algorithm takes these floodwater pixels as cloud shadows directly to reduce the false detection. However, some real floodwater may be mistakenly taken as shadows too, which increases the omission errors.

The water reference map may not cover some new reservoirs or hydraulic projects. Therefore, these reservoirs may be falsely assigned as floodwater rather than normal water. The water reference map used by the VFM should be updated every year.

All the above water detection errors are included in water fraction retrieval accordingly. Besides these error sources, water fraction retrieval can be affected by other factors such as sensor noises and measurement uncertainties. Some floodwater with some very thin cloud cover or smoke can still be detected in the VIIRS flood maps due to the strategy to detect as much water as possible used by VFM algorithm. However, the contamination from the cloud cover and smoke may result in underestimation of water fractions than actual ones.

Anisotropy is the major error source for water fraction retrieval, resulting in underestimate of both water detection and water fraction retrieval on the scan edges. Although the DNNS method uses the nearest neighboring pixels to derive reflectance of pure land and pure water dynamically, the water fraction retrieval is still systematically affected by the anisotropy effect, which might contribute about 10% variance to the retrieved water fractions. This part should be the major improvement on the VFM algorithm in future.

Other factors such as sensor noises and measurement uncertainties can also affect water detection and water fraction retrieval. However, the VFM algorithm is designed with large tolerance to these uncertainties. These factors may only contribute limited variance (within 5%) to the water fractions.

2.6 Practical Considerations

2.6.1 Numerical Computation Considerations

The VFM algorithm is overall pixel-based, which does not require much computation considerations. However, the VFM algorithm includes six major processes, which takes a lot of computation. The object-based terrain shadow removal requires clustering the adjacent water pixels into a water object or polygon. In very rare situations, the recursion process may cause problems for very large water objects. Therefore, during the recursion process to search for water pixels, the recursion is terminated when the number of the searched pixels meets the pre-defined conditions. The change detection method is widely used in the VFM process such as snow/ice detection, supra-snow/ice water detection, and minor water detection. To save computation resource, the calculated variables from the nearest neighboring moving window centering at one pixel are applied to all the pixels nearby within half moving window size to the centering pixel. Although it might decrease the accuracy slightly, it helps save the computation resources substantially.

2.6.2 Programming and Procedural Considerations

The VFM includes NRT process, daily composition process and 5-day composition process. The NRT process includes granule process and NWS domain process, and the NWS domain process needs multiple granules to get a mosaicked file with a latency requirement about 40 minutes. However, in NDE environment, it is difficult to request the previous granules for the current granule process, which brings difficulty to determine whether a NWS domain is completed. When incorporating the codes in NDE environment, a NWS domain is determined to be completed when the VIIRS granules change between ascending and descending.

2.6.3 Quality Assessment and Diagnostics

Along with the flood detection results, quality flags are also output by the VFM products to record the quality of the detection and fraction retrieval. The quality flags are defined in the following types:
- **Low quality flag (2):** If a pixel is detected as cloud, but in the VIIRS enterprise cloud mask, it is shown as clear-sky land, then this pixel is with low quality flag. If a pixel is detected as non-cloud, but in the VIIRS enterprise cloud mask, it is shown as cloud, then this pixel is with low quality flag. All the cloud shadow pixels on the granule edges with their clouds in other granules are with low quality flag.
- **Moderate quality flag (1):** Pixels that are detected as vegetation, bare land or water with the DT algorithm, but are re-detected as a different type during the post analysis are with moderate quality flag.
- **Fill value (255):** All the pixels with fill value from the detection results are with fill-value quality flag.
- **High quality flag (0):** The rest pixels that are not with any of the above three quality flags are with high quality flags.

The VFM fills the dataset with fill values in the following situations:
- **Bad data from SDR in any channel that is used by VFM:** Those scans with fill value 65533 are all taken as fill value in the VFM output.
- **Scans with solar eclipse:** Scans with solar eclipse from the SDR record are with fill value.

- **Data with solar zenith angles beyond the defined range:** Pixels with solar zenith angle beyond the defined range are with fill value. The range of solar zenith angle (θ) is defined based on days of year (DOY):
  - If: $1 \leqslant DOY \leqslant 59$, or $291 \leqslant DOY \leqslant 366$, then in the north hemisphere, $\theta \leqslant 85°$, and in the south hemisphere, $\theta \leqslant 76°$
  - If $60 \leqslant DOY \leqslant 99$, or $251 \leqslant DOY \leqslant 290$, then $\theta \leqslant 80°$ globally.
  - If $100 \leqslant DOY \leqslant 250$, then in the north hemisphere, $\theta \leqslant 76°$, and in the south hemisphere, $\theta \leqslant 85°$
- **Data with sensor zenith angles above 70°:** Pixels with sensor zenith angles above 70° are with fill value.
- **Data with calibrated reflectance or brightness temperature out of valid range:** Pixels with calibrated reflectance or brightness temperature out of valid range are with fill value.
- **Other abnormal data:** Pixels with abnormal reflectance in either of the Vis, NIR and SWIR channels are with fill value. For example, pixels that meet either of these abnormal situation: $R_{SWIR} - R_{Vis} \geqslant 50\%$, or $R_{SWIR} - R_{NIR} \geqslant 40\%$, or $R_{Vis} - R_{NIR} \geqslant 40\%$, are with fill value.

2.6.4 Exception Handling

There are altogether 32 error types defined to handle processing exceptions such as memory check, file access status check, file name check, file I-O success check and so on. For each module, a log file is defined globally to record all the error types during the process. VFM does not output any results if a granule meets either of the following conditions:

- It is a nighttime granule.
- It is a granule near North Pole or South Pole.
- It is a granule with valid data less than 20%.

2.7 Validation

The VFM algorithm and products have been validated through visual inspection, comparison with MODIS flood products and radar flood products, and quantitative validation with Landsat-8 OLI images.

2.7.1 Visual inspection

The VFM product has been evaluated offline with VIIRS imagery since 2015. Over 10,000 VIIRS granules have been tested and visually inspected with VIIRS false-color images composited with VIIRS Imager bands 3 (Red), 2 (Green) and 1 (Blue). These granules cover most of the global land areas between 80°S and 80°N year-round. Visual inspection consistently shows promising product performance. Fig. 2-22 depicts an example of visual inspection validation. Fig. 2-22(*a*) is a VIIRS false-color image on 19 May 2015 at 2135 UTC in north Alaska, and the corresponding VIIRS flood detection map is shown in Fig. 2-22 (*b*). In Fig. 2-22 (*a*), the cyan color indicated there were still snow cover in that area with some clouds (shown in light grey-white) and cloud shadows (darker grey). In the southeast part of the image, the topography causes some dark terrain shadows. During northern Alaska's break-up and snow-melting season, ice jams and snowmelt on top of the snow/ice surface often causes flooding. The situation in Fig. 2-22 (*a*) is a complex scene, yet Fig.

2-22 (*b*) shows realistic results from the VFM product. Clouds are masked in grey, snow cover is flagged in white, river/lake ice is detected in cyan, and shadows are removed and shown in dark grey. Water is divided into two types: supra-snow/ice water and supra-veg/bare land water. The Supra-snow/ice water in Fig. 2-22 (*b*) shown in purple indicates either of the three situations: 1) water sitting on top of river/lake ice; 2) Ice in semi-transparent status due to melting; 3) Mixed ice & water. Supra-veg/bare soil floodwater are represented in water fractions (from light green to red), and the rest clear-sky land including vegetation and bare soil is shown in brown. Overall, the product performs well under complex weather and ground conditions.
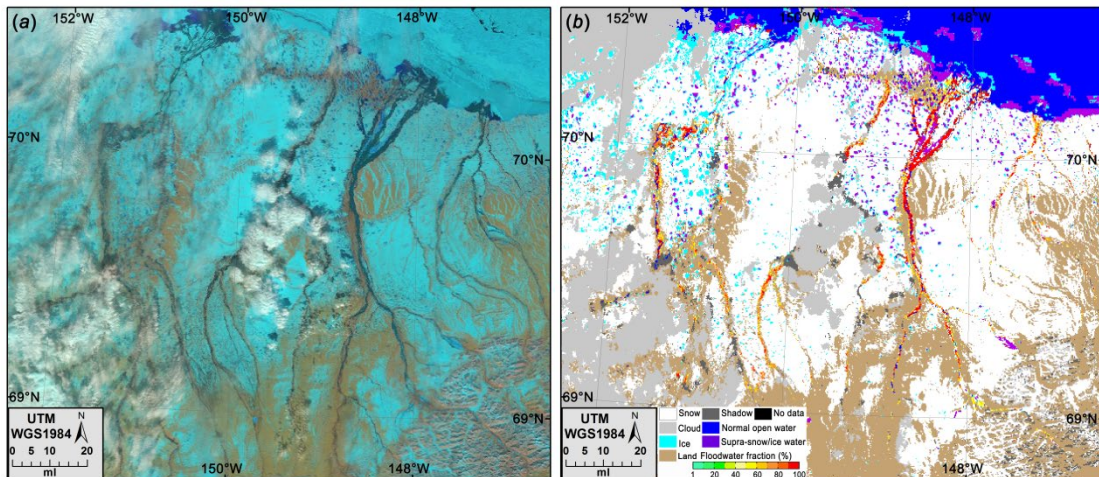

Fig. 2-22 (*a*) SNPP/VIIRS false-color composite image in north Alaska on 19 May2015 2135 UTC; (*b*) SNPP/VIIRS flood detection map in north Alaska on 19 May2015 2135 UTC

2.7.2   Comparison with MODIS flood products

MODIS experimental flood products were publicly released in 2011 by NASA based on Dartmouth's flood detection algorithms and are available in 2-day, 3-day and 14-day composite flood maps at the website http://oas.gsfc.nasa.gov/floodmap. During some flood events, daily near real-time (1-day) flood maps are also available in this website. To remove cloud shadows and terrain shadows, a composition process is applied based on multiple-day flood maps. This process sometimes misclassifies floodwater as shadows and under-reports floodwater in MODIS 2-day and 3-day composite flood maps. The VFM algorithm removes cloud shadows and terrain shadows on each overpass and therefore is able to produce near real-time flood maps with less shadow bias. Fig. 2-23 presents an example showing the difference between the two flood products during California's flood in January 2017. Fig. 2-23 (*a*) is MODIS false-color composite image on 11 Jan. 2017 at 1910 UTC downloaded from the MODIS Today website (http://ge.ssec.wisc.edu/modis-today), Fig. 2-23 (*b*) is a MODIS flood map using 1-day, 2-day and 3-day composited floodwater shapefiles downloaded from the website http://oas.gsfc.nasa.gov/floodmap. In Fig. 2-23 (*b*), blue is floodwater in MODIS 3-day composited floodwater layer from 09-11 Jan. 2017, green and blue represent floodwater in MODIS 2-day composited floodwater layer from 10-11 Jan. 2017, and red, green and blue show MODIS 1-day near real-time floodwater on 11 Jan. 2017 at 1910 UTC. Suomi-NPP/VIIRS false-color composite image and the corresponding automatic flood detection map on 11 Jan. 2017 at 2116 UTC produced by VFM algorithm are shown in Fig. 2-23(*c*) and (*d*), respectively.

In the MODIS false-color image (Fig. 2-23 (*a*)), floodwaters are visible as dark blue. These floodwaters are successfully identified in the MODIS 1-day floodwater layer (red, green and blue in Fig. 2-23 (*b*)). However, many cloud shadows and terrain shadows are misclassified as floodwaters. The composition process results in fewer cloud shadows in the 2-day composite floodwater layer (green and blue in Fig. 2-23 (*b*)), but much of the valid floodwater identified in the 1-day floodwater layer is removed. Further, the 3-day composite floodwater layer (blue in Fig. 2-23 (*b*)) has almost no shadows, but almost all of the floodwater is removed as well. Weather conditions changed slightly between the 1910 UTC Terra-MODIS overpass and the 2116 UTC SNPP-VIIRS overpass, and the change of cloud cover results in some different areas where floodwater is obscured by clouds. Despite the complex conditions depicted in the VIIRS false-color composite image Fig. 2-23(*c*), the VFM results (Fig. 2-23(*d*)) are still highly consistent with the false-color composite image. Overall, floodwater detected in VIIRS flood map corresponds well with the flooding apparent in the imagery as well as the 1-day MODIS floodwater layer. Cloud shadows and terrain shadows (dark grey in Fig. 2-23 (*d*)) have been separated from floodwater in the VFM flood product much better than in the MODIS flood product.

Two days later, on 13 Jan. 2017, clear skies offered a good view of the flooding in California. Because there were clear skies on 11 Jan. and 13 Jan. 2017, but partially cloudy skies on 12 Jan. 2017, MODIS 2-day composite floodwater layer from 12-13 Jan. (green and blue in Fig. 2-24(*a*)) show similar floodwaters to that in the 3-day (from 11 Jan. to 13 Jan.) composite floodwater layer (blue in Fig. 2-24(*a*)). However, around the mountains especially in the south region, some terrain shadows erroneously appear as floodwaters in MODIS 2-day composite floodwater layer. With further composition process, most terrain shadows in the 2-day composite floodwater layer disappeared in the MODIS 3-day composite floodwater layer. Comparing with MODIS flood products, similar floodwater distribution was depicted, but terrain shadows along the mountains are accurately identified in VFM flood map (Fig. 2-24 (*b*)).

To quantitatively analyze the difference between the two flood products, MODIS floodwater datasets in California on Jan. 11 and Jan. 13, 2017 are resampled to 375-m spatial resolution to compare with VIIRS flood datasets in a pixel-to-pixel way. It was completely clear-sky in California flooding regions on Jan. 13, 2017, and flood situation remained similar to Jan. 11. By visual inspection between VIIRS flood detection result and VIIRS false-color image on that day, VIIRS floodwater detection rate reached above 95%. Therefore, VIIRS floodwater dataset on Jan. 13 is used as a reference map to indicate the actual floodwater extent in moderate-resolution satellite imagery. The total number of floodwater pixels (N_{total}) is calculated from MODIS near real-time (1-day), 2-day composited, 3-day composited floodwater datasets and VIIRS near real-time floodwater datasets. If a floodwater pixel is also shown in the reference map, then it is taken as a true floodwater pixel, and N_t represents the total number of rue floodwater pixels. If a flood pixel in the reference map shown as clear-sky land in MODIS or VIIRS flood maps, then it is taken as an undetected floodwater pixel, and the total number of undetected floodwater pixels is N_u. False detection ratio P_f, detection accuracy rate P_t, and omission ratio (undetected ratio) P_O are calculated in Equations (2-43), (2-44) and (2-45) respectively:

$$P_f = \frac{N_{total} - N_t}{N_{total}} \times 100\% \tag{2-43}$$

$$P_t = \frac{N_t}{N_{total} + N_u} \times 100\% \tag{2-44}$$

$$P_O = \frac{N_u}{N_t + N_u} \times 100\% \tag{2-45}$$

Table 2-6 lists the results on the Jan. 2017's California flood event from MODIS and VIIRS. From Table 2-6, MODIS flood map on Jan. 11, 2017 detected altogether 135797 flood pixels, but only 33937 pixels are real floodwater pixels and 10247 flood pixels remained undetected. False detection ratio was about 75%. With 2-day composition process, only 22384 flood pixels were detected, of which 17594 pixels were real flood pixels. Comparing to MODIS near real-time flood map, false detection ratio with 2-day composition process decreased to 21.4%. However, undetected flood pixels reached 26590, resulting in 60.18% omission ratio. After 3-day composition process, only 1435 flood pixels were detected, of which 1285 pixels are real flood pixels. False detection ratio decreased to 10.45%, but undetected flood pixels increased to 42899, and omission ratio reached 97.09%. With more clear-sky weather conditions on Jan. 13, MODIS showed better detection result. In MODIS 2-day composite flood map, altogether 34387 flood pixels were detected, of which 26208 pixels were real flood pixels. About 15124 flood pixels were undetected. False detection ratio and omission ratio were 23.79% and 36.59% respectively. With 3-day composition process, MODIS results showed 29572 detected flood pixels, 25844 real flood pixels and 15488 undetected flood pixels. False detection ratio and omission ratio were 12.61% and 37.47% respectively. VIIRS near real-time flood map on Jan. 11, 2017 detected 25258 flood pixels, of which 25077 pixels were real flood pixels. About 6762 flood pixels were not detected, which were mainly caused by the uncertainty of cloud detection. False detection ratio was only 0.72% and omission ratio reached 21.24%. Comparing to MODIS flood products, the detection accuracy is much better in both complex weather conditions with cloud cover and clear-sky conditions. The improved performance especially on cloud shadow and terrain shadow removal guarantees the near real-time flood detection capability of VFM algorithm and the quality of VFM products.
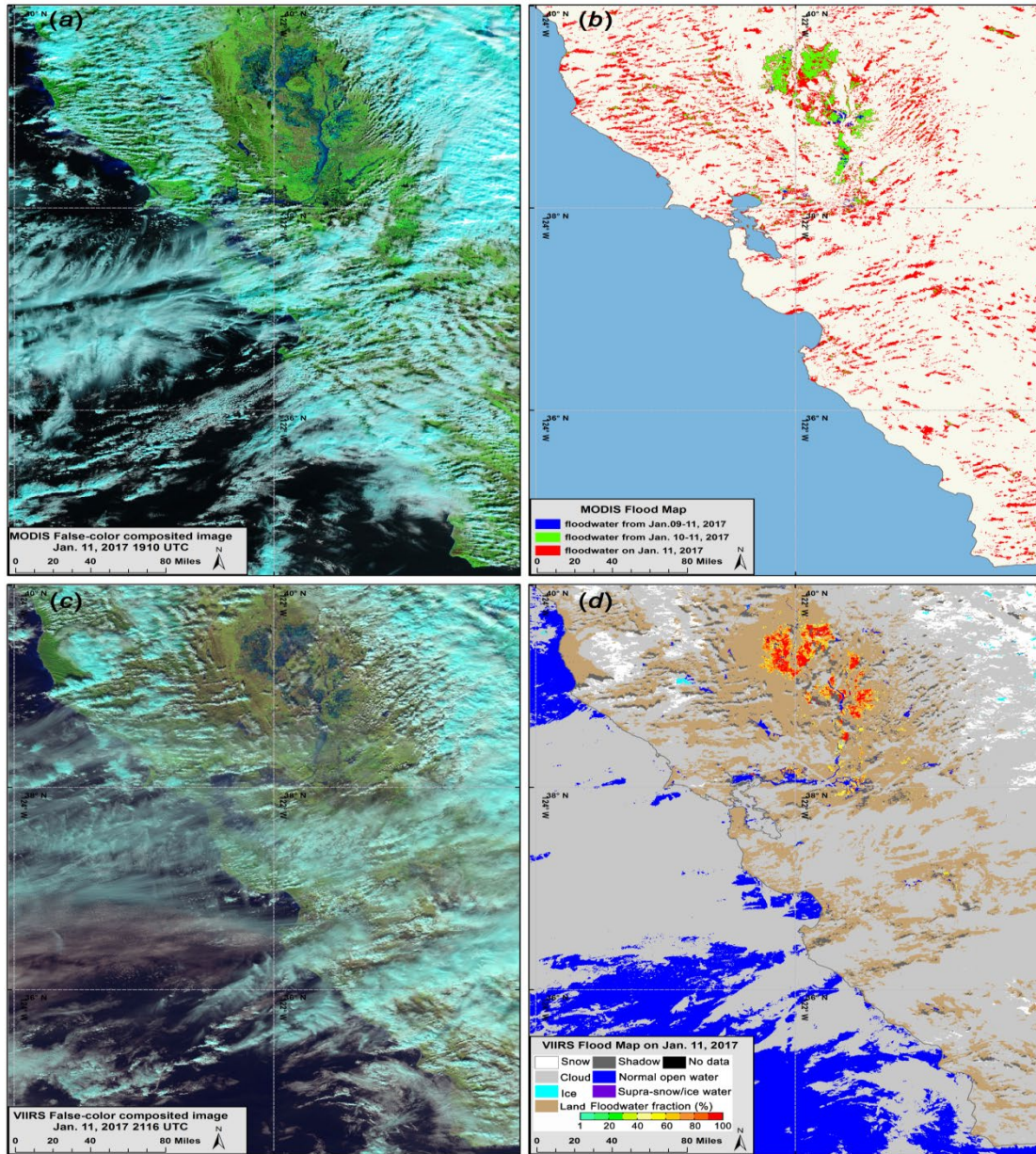
Fig. 2-23 (*a*) MODIS false-color composite image on 11 Jan. 2017 at 1910 UTC; (*b*) MODIS near real-time, 2-day and 3-day composited flood map in California, USA on 11 Jan. 2017; (*c*)SNPP/VIIRS false-color composite image on 11 Jan. 2017 at 2116 UTC; (*d*) SNPP/VIIRS near real-time flood map produced by VNG Flood V1.0 on 11 Jan. 2017 at 2116 UTC
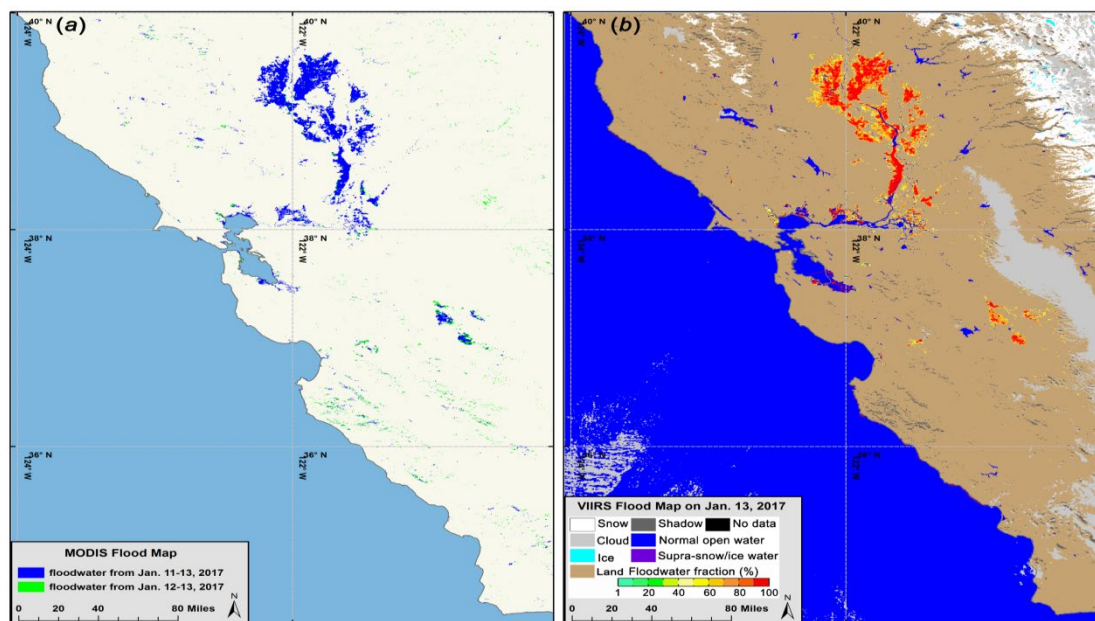
Fig. 2-24 (*a*) MODIS 2-day and 3-day composited flood map in California, USA on 13 Jan. 2017; (*b*) SNPP/VIIRS flood map produced by VNG Flood V1.0 on 13 Jan. at 2038 UTC

Table 2-6 Comparison between MODIS flood product and VIIRS flood product

	Dates	Composition	N_{total}	N_t	N_u	P_f (%)	P_t (%)	P_O (%)
MODIS	Jan. 11	near real-time	135797	33937	10247	75.01	23.24	23.19
		2-day composite	22384	17594	26590	21.40	35.93	60.18
		3-day composite	1435	1285	42899	10.45	2.90	97.09
	Jan. 13	2-day composite	34387	26208	15124	23.79	52.93	36.59
		3-day composite	29572	25844	15488	12.61	57.35	37.47
VIIRS	Jan. 11	near real-time	25258	25077	6762	0.72	78.32	21.24
	Jan. 13	near real-time	42499	42499	–	–	–	–

2.7.3   Comparison with radar flood products

Radar imagery is very popular in flood mapping because it can penetrate cloud cover. Radar flood products are good reference for evaluating flood products from other satellite imagery. The radar flood products from Sentinel-1 and Radarsat have been used to evaluate with VFM products during many major flood events such as the 2017's hurricane Harvey flood, the 2019's hurricane Florence flood, the 2019's Midwest flood, and floods in Somalia, south Asia and so on. The radar flood maps are mainly from the website of WMO's International Charter (https://disasterscharter.org). Overall, the radar flood products have much higher spatial resolution than the VIIRS flood products. For floods caused by intensive rainfall, the radar flood products can present flood extent under cloud cover, whereas the VFM products fail to detect. Overall, under clear-sky coverage, the VIIRS flood maps show consistent results to the radar flood products.

However, over land types with vegetation cover, the radar flood products detect less flood extent than the VIIRS flood products, and over wet barren lands, radar flood products may detect more false floodwater than the VIIRS flood products. Fig. 2-25 presents an example in the West Gulf region of USA during the 2017's hurricane Harvey. Fig. 2-25 (A) is a Sentinel-1 flood map on Aug. 31, 2017 downloaded from International Charter's website, and Fig. 2-25 (B) is a VIIRS flood map on the same day in the same region. The two flood maps show similar flood extent in most regions, but overall the VIIRS results show larger flood extent, especially over regions with vegetation cover. Fig. 2-25 (C) is a subset of Fig. 2-25 (A) and Fig. 2-25 (E) is a subset of Fig. 2-25 (B). Fig. 2-25 (D) is an aerial photo taken on Sep. 02, 2017 in the subset region of Fig. 2-25 (C) and (E). From Fig. 2-25 (D), this region was mostly inundated and most floodwater was veiled by vegetation cover. The Sentinel-1 flood map (Fig. 2-25 (C)) only showed very small flood extent, and failed to detect most floodwater partially veiled by vegetation cover. In comparison, although the VIIRS flood map missed some floodwater that were completely veiled by vegetation cover and underestimated the floodwater fractions due to the impact from vegetation cover, it successfully detected most of the floodwater, which might reflect more robust detection capability of VIIRS imagery over vegetation cover than radar imagery.

Fig. 2-26 shows a comparison example between Radarsat flood map and VIIRS flood map in Somalia during the May 2018's flood. Fig. 2-26 (a) is a Radarsat flood map on May 09, 2018 in Somolia downloaded from Charter's website. Fig. 2-26 (b) is a natural color image from Sentinel-2B on May 08, 2018, Fig. 2-26 (c) is a VIIRS flood map on May 07, 2018 and Fig. 2-26 (d) is the VIIRS natural color image on May 07, 2018 in the same region of Fig. 2-26 (a). From Fig. 2-26 (a), it showed large flood extent in Somalia. However, in the corresponding VIIRS flood map (Fig. 2-26 (c)) no significant floodwater was detected. By comparing with the VIIRS's natural color image (Fig. 2-26 (d)), no significant floodwater could be found in this region. A Sentinel-2B natural color image on May 08, 2018 (Fig. 2-26 (b)) was obtained for further comparison, in which no significant floodwater was found in the region too. By analyzing the Radarsat flood map with Sentinel-2B image, it is found that the falsely detected floodwater was mostly over barren land. Due to the rainfall during previous days, these barren soils were wet and thus looked darker than those dryland, but they were not in flooding at all. The comparison proves that VIIRS flood maps show steady and robust detection over these special situations, which may be used as a good supplement resource for flood mapping.
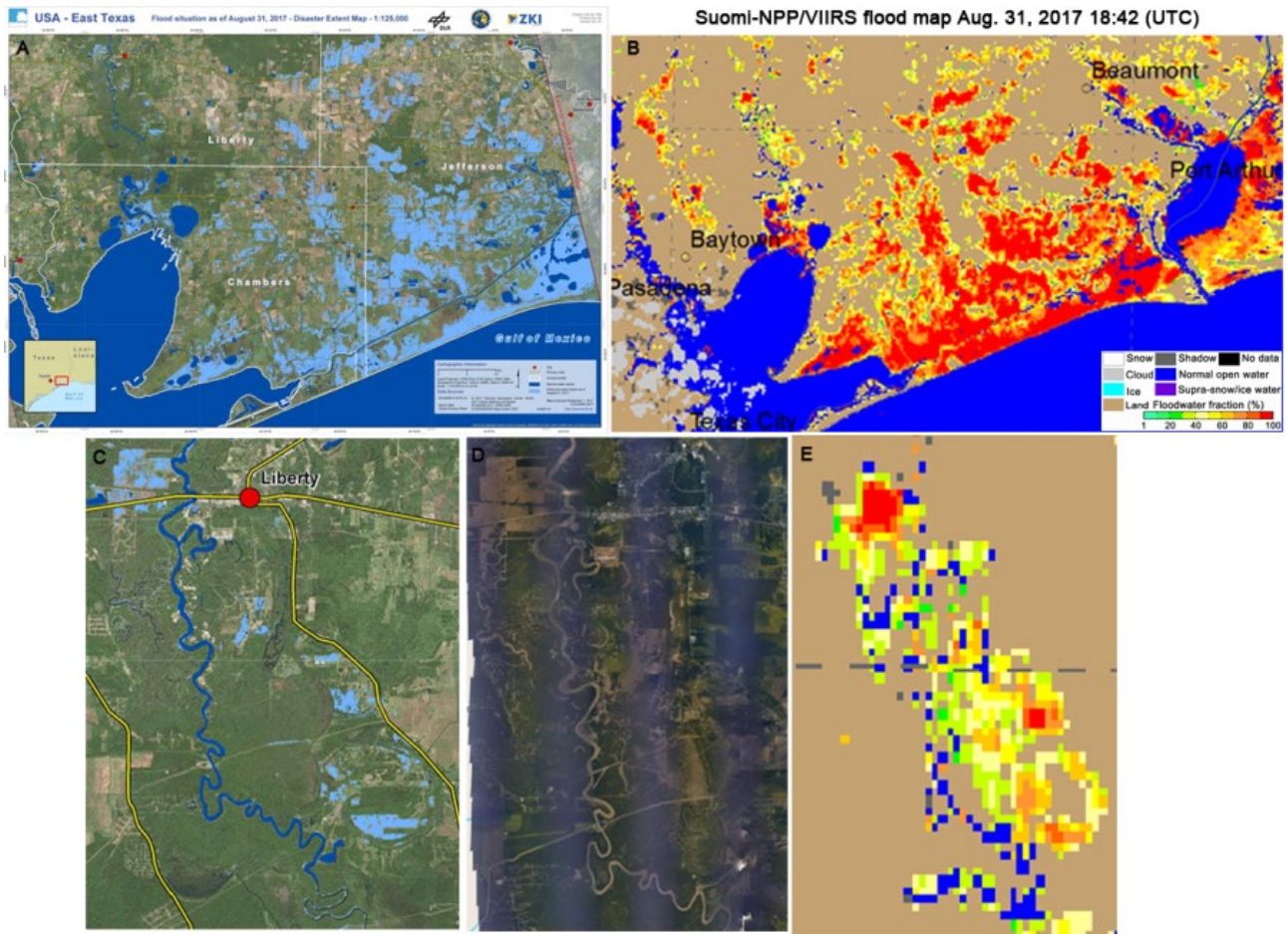
Fig. 2-25 Flood maps from Sentinel-1 and VIIRS in the West Gulf region during 2017's hurricane Harvey (A) Sentinel-1 flood map on Aug. 31, 2017; (B) SNPP/VIIRS flood map produced by VNG Flood V1.0 on Aug. 31, 2017; (C) A subset of (A); (D) Aerial photo taken on Sep. 02, 2017 in the subset region of (C); (E) A subset of (B)
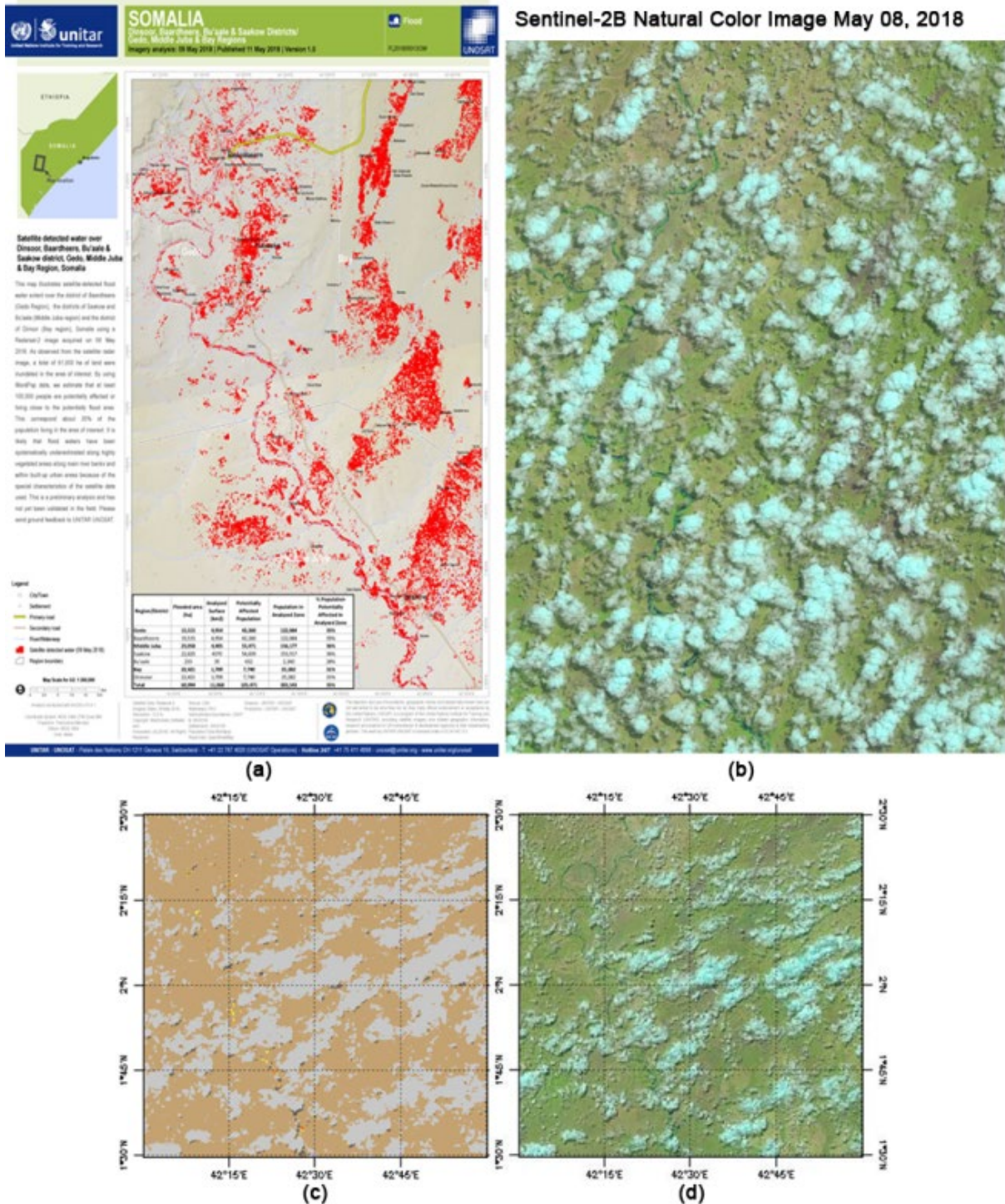
Fig. 2-26 Flood maps and images from Radarsat, Sentinel-2B and Suomi-NPP/VIIRS in Somalia during the May 2018's flood (A) Radarsat flood map on May 09, 2018; (B) Sentinel-2B natural color image on May 08, 2018; (C) SNPP/VIIRS flood map produced by VNG Flood V1.0 on May 07, 2018; (D) SNPP/VIIRS natural color image on May 08, 2018

2.7.4 Validation against Landsat-8 OLI imagery

Landsat-8 OLI imagery is a good data source to validate VIIRS flood product. The validation is done in two ways: 1) overlapping VIIRS flood products on Landsat-8 OLI images at 30-m resolution; 2) degrading Landsat-8 OLI images to 375-m resolution for comparison with VIIRS. The first way can be done via SSEC's Real Earth (http://realearth.ssec.wisc.edu/) visualization tool. Here, the near real-time availability of both VIIRS flood products and Landsat-8 OLI images in the web browser interface make it easy to overlap products and imagery. The Landsat-8 OLI images have been utilized for validation since 2015 globally, and the validation results are quite promising. Fig. 2-27 presents an example in Texas on 06 June 2016. Fig. 2-27(*a*) is a Landsat-8 OLI image from 1650 UTC where dark blue areas are floodwater. The VIIRS flood map from 1943 UTC is a semi-transparent overlay on top of the OLI image in Fig. 2-27(*b*). From Fig. 2-27, although cloud conditions are slightly different between the two observations, over clear-sky regions, VIIRS flood detection results were consistent with the high-resolution Landsat-8 OLI imagery. Most floodwater was accurately detected in the VIIRS flood map with larger water fractions (more red) in VIIRS flood map corresponding with more flooding water (more dark blue) in Landsat-8 image. This type of performance is typical in the other Landsat/SNPP validation comparisons.
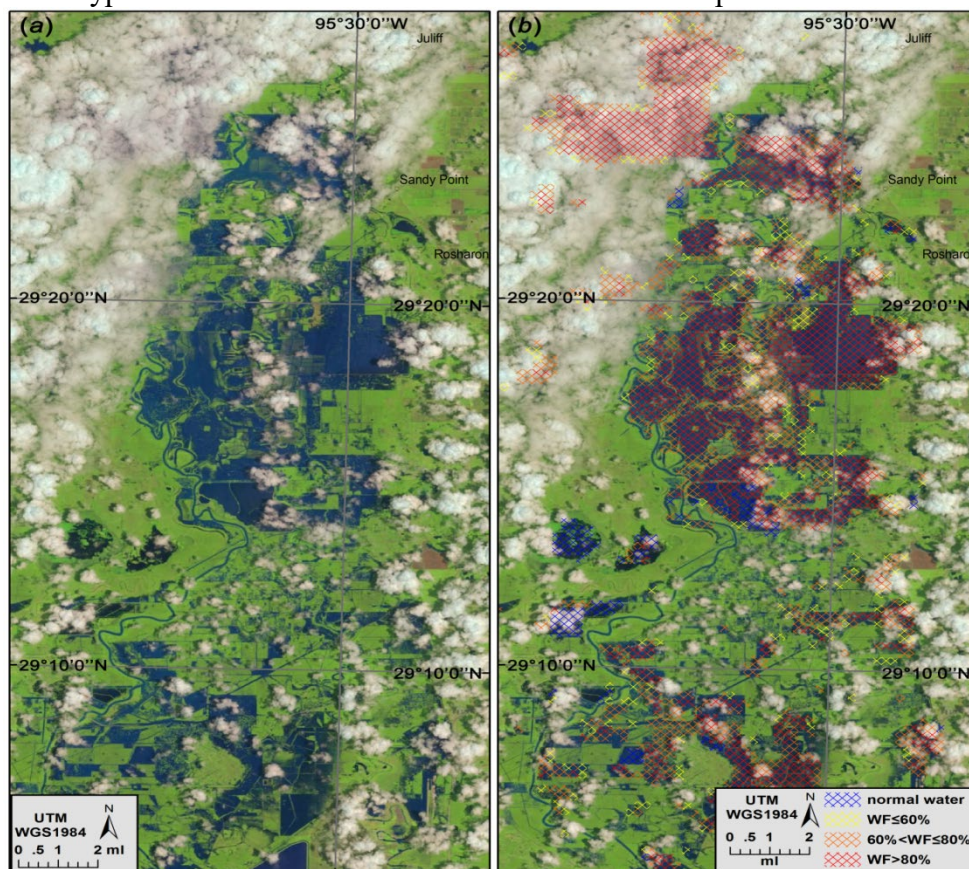

Fig. 2-27 (*a*) Landsat-8 OLI false-color composite image in Texas, USA on 06 June 2016 at 1650 UTC; (*b*) VIIRS flood detection map on 06 June 2016 at 1943 UTC overlaid on top of the OLI image from Fig. 2-27(*a*)

To provide quantitative validation, Landsat images are remapped to 375-m resolution for comparison with VIIRS flood maps. The comparisons are limited due to different image modelling, calibration, geolocation accuracy for satellite images at different spatial resolution, viewing geometry, and overpass times (Schroeder et al., 2008; Li. et al., 2012). More than 10 Landsat 30-m images were remapped to spatially match with VIIRS flood detection results. Cases were selected to include supra-veg/bare soil floods and supra-snow/ice floods. In Landsat images, water was extracted interactively to generate 30-m water masks, and then water fractions were calculated at 375-m grids to compare against VIIRS water fraction maps. Fig. 2-28 presents three pairs of flood maps between 375-m remapped Landsat flood maps and VIIRS flood maps. Fig. 2-28(*a*) is a resampled Landsat-7 ETM 375-m water fraction map on 13 Jan. 2013 in Sacramento Valley of California, USA and its correspondent SNPP/VIIRS flood map is shown in Fig. 2-28(*b*). Fig. 2-28(*c*) and Fig. 2-28(*d*) are another pair of flood maps from Landsat-7 ETM (Fig. 2-28(*c*)) and Suomi-NPP/VIIRS (Fig. 2-28(*d*)) on 13 Jan. 2017 in California. Fig. 2-28(*e*) presents a 375-m water fraction map from Landsat-8 OLI on 01 April 2015 along the Sag River in northern Alaska, USA, and the same day's SNPP/VIIRS flood map in the same region is shown in Fig. 2-28(*f*). From Fig. 2-28, VIIRS flood maps show similar floodwater distribution with Landsat flood maps, especially in regions with large water fractions. However, there are more small-water-fraction floodwater locations in the Landsat flood maps than in the VIIRS flood maps. This is reasonable because the signals from land are much stronger than from water when water fraction is small. Mixed water pixels in VIIRS imagery contain a smaller signal than in Landsat imagery due to the imager resolution and therefore it is expected that VIIRS – or any imager with similar spatial resolution - would have difficultly detecting mixed water pixels with low water fractions. Another issue is that for pixels with neighboring water pixels in large water fractions, the water fraction retrieval of these pixels shows larger results than Landsat. This difference may be caused by the difference between VIIRS and Landsat in image modelling, geolocation accuracy and viewing geometry.
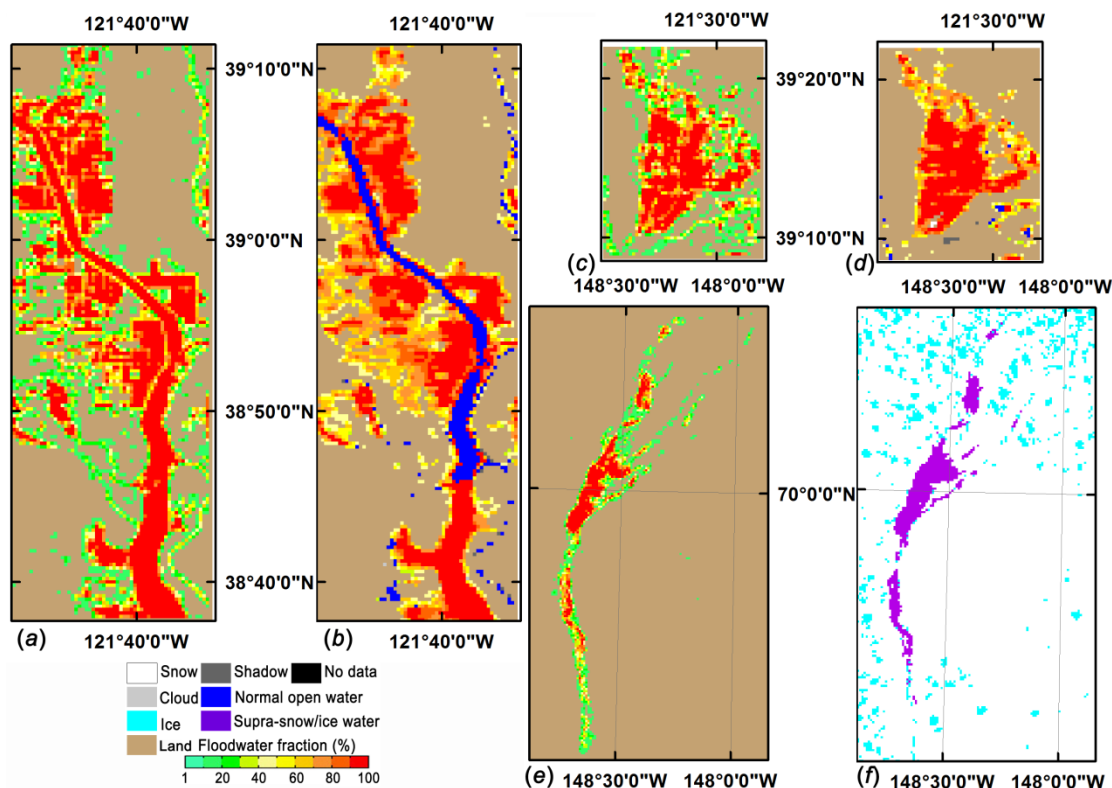
Fig. 2-28 Three pairs of flood maps for comparison between SNPP/VIIRS and Landsat imagery: (a) Landsat-7 ETM on 13 Jan. 2017 in California, USA, (b) the correspondent SNPP/VIIRS flood map of (a); (c) Landsat-7 ETM on 13 Jan. 2017 in California, USA, (d) the correspondent SNPP/VIIRS flood map of (c); (e) Landsat-8 OLI on 01 April 2015 along the Sag River in Alaska, USA, (f) the correspondent SNPP/VIIRS flood map of (e)

For further validation, |D_WF|, which is defined as the absolute water fraction difference between Landsat and VIIRS, is calculated and statistics of percentages of |D_WF| with different ranges are applied to reflect detection and retrieval accuracy. For supra-veg/bare soil floodwater, percentages are calculated in three types: 1) |D_WF| < 100%; 2) |D_WF| < 30%; 3) |D_WF| < 20%. The first type actually ignores water fraction difference between Landsat and VIIRS and thus reflects water detection accuracy, and the rest two types indicate water-fraction retrieval accuracy. For supra-snow/ice water without water fraction retrieval, only the first type is calculated to derive the general detection accuracy. About 50,000 valid samples were collected on supra-veg/bare soil floodwaters and 10,000 samples for supra-snow/ice water from about 10 Landsat images and VIIRS flood maps. Fig. 2-29 presents the validation results of supra-veg/bare soil water detection, and the results of supra-snow/ice water detection is shown in Fig. 2-30. From Fig. 2-29 and Fig. 2-30, water detection and fraction retrieval accuracy increase with water fractions, which is consistent to the results shown in Fig. 2-28 with better consistency over larger water fractions. For supra-veg/bare soil water, with water fractions larger than 80%, the detection accuracy is about 95%, water-fraction retrieval accuracy with |D_WF| less than 30% is above 90%, and water-fraction retrieval accuracy with |D_WF| less than 20% is above 80%. When water fractions are below 40%, water detection accuracy is much higher than water-fraction retrieval accuracy, which somehow reflects there are

more uncertainties in the DNNS method in water fraction retrieval over pixels with small water fractions. Detection percentage of supra-snow/ice water reaches about 80% when water fractions are above 80%, and increases more linearly with water fractions than supra-veg/bare soil water detection. Overall, percentages of supra-snow/ice water detection are about 20% less than supra-veg/bare soil water detection. This might be related to the higher reflectance of snow/ice surface than vegetation and bare soils in visible to near infrared channels. The stronger signals of snow/ice surface may bring about larger uncertainties on water detection.
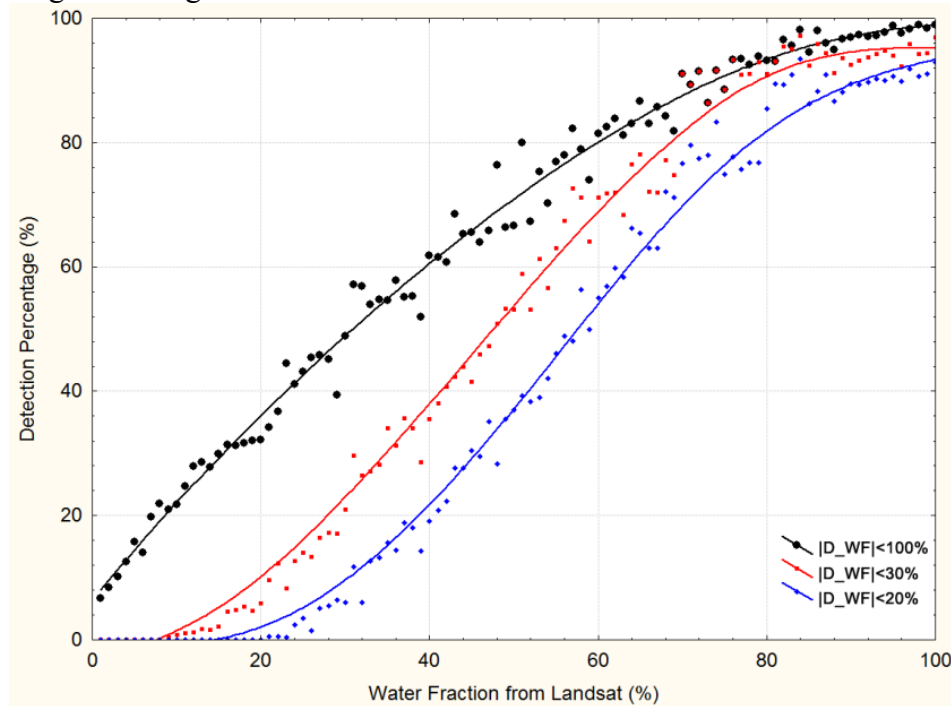

Fig. 2-29 Scatter plot of supra-veg/bare soil water detection percentage of VIIRS over water fractions from Landsat imagery
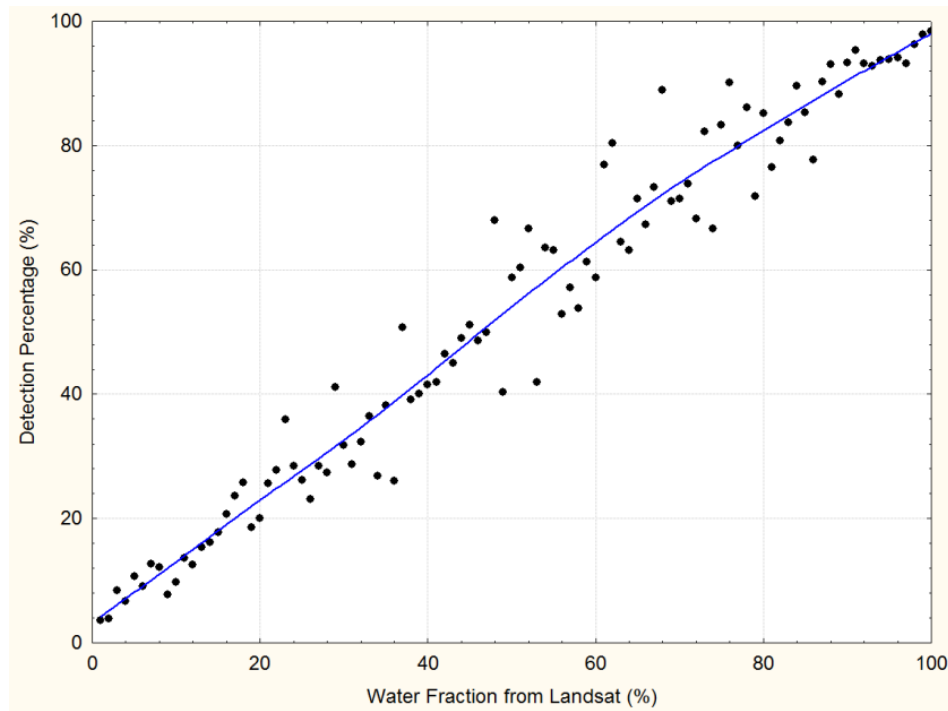
Fig. 2-30 Scatter plot of supra-snow/ice water detection percentage of VIIRS over water fractions from Landsat imagery

3   ASSUMPTIONS AND LIMITATIONS

The VFM product is a daytime-only product and the algorithm is developed based on the following assumptions:
- The reflectance of water surface without sun-glint contamination in the SWIR channel is close to 0 and varies little with suspending matter in comparison to the Vis and NIR channels, which allows this channel to be a key channel for water detection and water fraction retrieval.
- In neighboring regions, reflectance variance caused by anisotropy effect is similar in the Vis, NIR and SWIR channels.
- Ignoring cloud thickness, one cloud pixel at most cast one cloud shadow pixel in the VIIRS 375-m imagery, which is used as the base to construct one-to-one relationship between cloud and cloud shadow.
- Floodwater generally accumulates in low-lying topography with small surface roughness, and terrain shadow mainly forms in mountainous region with large surface roughness, which is used as the base for terrain shadow removal.

These assumptions lay the foundation of the VFM algorithm. However, there are some exceptions for these assumptions. Although the SWIR channel is quite effective in water detection, it is with low reflectance over snow/ice surface as well. Thus, it is not utilized for supra-snow/ice water detection. The channel also brings confusion to the water detection over situations such as vegetation with some thin smoke, urban land with aerosol or thin snow cover, burnt scars with thin snow cover.

Anisotropy is not considered in the entire imagery, but the impacts on the Vis, NIR and SWIR channels are removed by using neighboring pixels for change detection and water fraction retrieval based on the assumption of similar anisotropy effect in neighboring regions. However, this can still cause problems in water detection and water fraction retrieval because of the reflectance variance in different regions. This might be the major issue of the current VFM algorithm.

Although the cloud shadow removal algorithm is developed based on the one-to-one assumption between cloud and cloud shadow, the assumption may not be applicable in high latitudes especially in seasons with large solar zenith angles, when cloud thickness cannot be ignored. Therefore, some cloud shadows may not be removed in VIIRS flood maps.

The surface roughness analysis is the base for terrain shadow removal. Nevertheless, some real water caused by melting water from glaciers may be taken as terrain shadows. This may happen quite common during summer time in high latitudes such as Alaska. Some terrain shadows can also be formed in flat topography in some regions with special topography conditions, and these shadows may not be removed from the VIIRS flood maps.

3.1   Performance Assumptions

It is assumed that only daytime VIIRS flood products are generated from Suomi-NPP and NOAA-20 over land regions between 80°S and 80°N in latitudes. Therefore, no VFM flood products are generated near North Pole and South Pole regions. Because the maximal solar zenith angle that VFM algorithm is applicable is set as 85°, in high latitudes during winter season, no VFM products are expected to be produced as well.

VIIRS is an optical sensor, and thus the VFM algorithm can only be used to detect flood under clear-sky coverage, which may cause some latency on flood detection if cloud conditions exist.

Under solar eclipse, because of sharply decreased reflectance from earth surface, the VFM algorithm is not applicable, and the scans with solar eclipse are not processed. Therefore, no VFM product under solar eclipse is produced in this situation.

For the same flood under the same cloud conditions, less water pixels with smaller water fractions are expected to derive in the granule edges than in nadir regions because of the anisotropy effect. Over floodwater with contamination from thin cloud and smoke, smaller water fractions are expected to derive in the VFM products.

On the edges between two granules, all the detected water pixels with the cloud positions out of the granule range are expected to be flagged as cloud shadow pixels to reduce the commission error based on the one-to-one relationship between cloud and cloud shadow.

Some terrain shadows especially along rivers may not be removed in the VIIRS flood maps because of small surface roughness of these shadows. This happens mostly in high latitudes.

The VFM mainly depends on its own cloud and snow/ice detection, although VIIRS enterprise cloud mask is applied. The four channels (I-band 01, 02, 03 and 05) used in VFM algorithm show limitations in detecting thin clouds and discrimination between ice cloud and snow/ice cover. Thus, in the VFM product, some thin clouds may not be detected, which results in unremoved cloud shadows from these clouds. Some ice cloud may be confused with snow/ice cover as well. Because the daily and 5-day composition process uses the maximal-water fraction and maximal-snow/ice cover scheme to composite the NRT flood maps, these errors are inherited in the daily and 5-day composited flood maps accordingly.

Overall, the VFM algorithm performs in a good balance among cloud, snow/ice, shadow and floodwater. It successfully detects most of moderate to major floodwater under clear-sky conditions, although it seems to make more mistakes in high latitudes especially in late fall season due to the complexity of ground and weather conditions.

3.2 Potential Improvements

With all the existing issues and errors in the current VFM algorithm, some potential improvements can be made to derive steadier results. The major potential improvements include anisotropy effect removal and implementing the cirrus channel (centering at 1.385μm) for better detection over thin cloud and ice cloud.

Anisotropy effect removal is one of the major improvements that can be made in future for steadier water fraction retrieval across the scan and between VIIRS images from Suomi-NPP and NOAA-20. Algorithm can be developed to stabilize the reflectance in the Vis, NIR and SWIR channels based on the geometry angles. With the improvement, the accuracy of water fraction retrieval can be improved about 5% to 10%.

Implementing the cirrus channel (VIIRS M-9) can help improve the detection accuracy on thin clouds and ice cloud. Currently, most residual cloud shadows in the VFM product are cast by unremoved thin cloud. With better detection from thin cloud, these errors can be fixed accordingly. Additionally, some floodwater with thin cloud contamination can be detected in the VFM product. Nevertheless, water fraction retrieval of this type of floodwater is affected resulting in under-estimated water fractions. The improvement of thin cloud detection can help discriminate this type of water, and corrections can be made accordingly on the water fraction retrieval.

Other potential improvement on the VFM product is to update the water reference map and land cover dataset. The water reference map should be updated with new reservoirs and hydraulic projects for less false floodwater alarm. The land cover dataset should be updated with land cover change from wild fires or new reservoirs.

In the current VFM product, there is no difference between disastrous floodwater and floodwater caused by agriculture activities such as rice paddy planting, which may bring about confusion to decision-makers. In future, differentiating disastrous floodwater from the VFM product can be another potential improvement for better assistance to decision-makers on disaster management.

4   REFERENCES

Ali, A., 1989.Study of river flood hydrology in Bangladesh with AVHRR data, Int.J. Remote Sens., vol. 10, pp. 1873–1892

Andrimont, R. D ,Bartholomé, E.&Defourny, P. (2012). 8 years water bodies monitoring analysis using MODIS over the Africancontinent. EGU General Assembly 2012, 12905

Barton, I. J.&Bathols,J. M. (1989).Monitoring floods with AVHRR,Remote Sensing of Environment, vol.30, no. 89–94

Brakenridge, G. R., Knox, J. C., Paylor, E. D., &Magilligan, F. J. (1994). Radar remote sensing aids study of the great flood of 1993,EOS Trans., AGU, 75(45), 521±527.

Brakenridge, G.R. & Anderson, E. (2006).MODIS-based Flood Detection, Mapping and Measurement: the Potential for Operational Hydrological Applications, Earth and Environmental Sciences, 72,1-12

Brakenridge, G R.(2011).Technical Description, DFO-GSFC Surface Water Mapping Algorithm,http://floodobservatory.colorado.edu/Tech.html

Brakenridge, G. R., Knox, J. C., Paylor, E. D., &Magilligan, F. J. (1994). Radar remote sensing aids study of the great flood of 1993, EOS Trans., AGU, 75(45), 521±527.

Carroll, M., Townshend, J.,DiMiceli, C.,Noojipady, P. &Sohlberg, R. (2009).A New Global Raster Water Mask at 250 Meter Resolution:, International Journal of Digital Earth, 2, 4

Ceccato, P., Flasse, S., and Gregoire, J.M.(2002). Designing a spectral index to estimate vegetation water content from remote sensing data: Part 2. Validation and applications. Remote Sensing of Environment 82: 198-207.

Croitoru, A., Crooks, A., Radzikowski, J., & Stefanidis, A. (2013). GeoSocial Gauge: A System Prototype for Knowledge Discovery from Social Media, International Journal of Geographical Information Science, 27(12): 2483-2508.

Cox, C.; Munk, W (1954). Statistics of the Sea Surface Derived from Sun Glitter. J. Mar. Res., 13, 198-227

Fisher, Adrian; Flood, Neil; Danaher, Tim (2016).Comparing Landsat water index methods for automated water classification in eastern Australia. Remote Sensing of Environment,Vol. 175,167-182

Gao, B. C. (1996). NDWI—A normalized difference water index for remote sensing of vegetation liquid water from space, Remote Sensing of Environment, 58:257-266 (1996)

Gumley, L.E. & King, M.D. (1995). Remote Sensing of Flooding in the U.S. Upper Midwest during the Summer of 1993, Bulletin of American Meteorological Society, 76, 6

Gupta, R. P. & Banerji, S. 1985. `Monitoring of reservoir volume using Landsat data', J. Hydrol., 77, 159±170.

Gupta, R. P. &Bodechtel, J. 1982. `Geotechnical applications of Landsat image analysis of Bhakra dam reservoir, India', RemoteSens. Environ., 12, 3±13.

Hutchison, K. D., Mahoney, R. L., Vermonte, E. F., Kopp, T. J., Jackson, J. M., Sei, A., and Iisager, B. D.(2009). A Geometry-Based Approach to Identifying Cloud Shadows in the VIIRS Cloud MaskAlgorithm for NPOESS, Journal of Atmospheric and Oceanic Technology 26: 1388–1397.

International Federation of the Red Cross and Red Crescent Societies (IFRC). *World Disasters Report*; Oxford University Press: Oxford, UK, 2008; ISBN 978-92-9139-156-1.

Jin, Y. Q. (1999). Flooding index and its regional threshold value for monitoring floods in China from SSM/I data. International Journal of Remote Sensing, 20(5): 1025-1030.

Johansson, A. M.& Brown, I. A. (2013). Adaptive classification of supraglacial lakes on the West Greenland ice sheet. IEEE Journal of Select Topics Appl. Earth Obs. Remote. Sens., 6(4), 1998-2007 (doi: 10.1109/JSTARS.2012.2233722)

Khlopenkov, K. V. and Trishchenko, A. P. (2007). New cloud, snow, and cloudshadow detection scheme for historical 1-km AVHHR data over Canada.*J. Atmos. Oceanic Tech.*, vol. 24, pp. 322–343.

Kundzewicz, Z.W.; Schellnhuber, H.J. (2004). Floods in the IPCC TAR perspective. *Nat. Hazards*, *31*, 111–128.

Lesson, A. A. Leeson, Shepherd, A., Sundal, A. V., Johansson, A. M., Selmes, N., Briggs, K., Hogg, A. E. &Fettweis, X. (2013). A comparison of supraglacial lake observations derived from MODIS imagery at the western margin of the Greenland ice sheet, Journal of Glaciology, Vol. 59, No. 218

Liang, Y.-L., Colgan, W., Lv, Q., Steffen, K., Abdalati, W., Stroeve, J., Gallaherb, D., Bayou, N. (2012). A decadal investigation of supraglacial lakes in West Greenland using a fully automatic detection and tracking algorithm, Remote Sensing of Environment, Volume 123, August 2012, Pages 127–138

Li, S. & Sun, D.(2013). Development of an integrated high resolution flood product with multi-source data, UMI Dissertations Publishing 2013, ISBN: 9781303635939, http://search.proquest.com/docview/1492669000, 2013

Li, S., Sun, D.L. & Yu,Y.Y. (2013). Automatic cloud-shadow removal from flood/standing water maps using MSG/SEVIRI imagery, International Journal of Remote Sensing, 34:15, 5487-5502

Li, S., Sun, D.L., Goldberg, M. D. &Sjoberg, B. (2015). Object-based Automatic Terrain Shadow Removal from SNPP/VIIRS Flood Maps, International Journal of Remote Sensing, Vol. 36, No. 21, 5504–5522

Li, S., Sun, D. L.,Yu, Y. Y.,Csiszar, I.,Stefanidis, A. & Goldberg, M. D. (2012).A New Shortwave Infrared (SWIR) Method for Quantitative Water Fraction Derivation and Evaluation with EOS/MODIS and Landsat/TM data, IEEE Transactions on Geoscience and Remote Sensing,99

Li, S., Sun, D.L., Goldberg, M. D&Stefanidis, A. (2013).Derivation of 30-m-resolution Water Maps from TERRA/MODIS and SRTM, Remote Sensing of Environment 134 (2013) 417–430

Liu, Yan Y,.Maidment, D. R., Tarboton, D. G., Zheng, X., Yildirim, A., Sazib, N. S., Wang, S. W. (2016). "A CyberGIS Approach to Generating High‐resolution Height Above Nearest Drainage(HAND) Raster for National Flood Mapping." CyberGISCenter Technical Report (2016).

Martinis, S., Twele, A., Strobl, C., Kersten, J., and Stein, E. (2013).A Multi-Scale Flood Monitoring System Based on Fully Automatic MODIS and TerraSAR-X Processing Chains. Remote Sensing, 5:5598-5619.

Martinis, S., Twele, A., and Voigt, S. (2009) Towards operational near real-time flood detection using a split-based automatic thresholding procedure on high resolution TerraSAR-X data, Nat. Hazards Earth Syst. Sci., 9, 303-314, doi:10.5194/nhess-9-303-2009.

Matgen, P., Schumanna, G., Henryc, J.-B., Hoffmanna, L. &Pfistera, L. (2007). Integration of SAR-derived river inundation areas, high-precision topographic data and a river flow model

toward near real-time flood management.International Journal of Applied Earth Observation and Geoinformation, 9, 247-263

Matgen, P., Hostache, R., Schumann, G., Pfister, L., Hoffmann, L., and Savenije, H. (2011). Towards an automated SAR-based flood monitoring system: lessons learned from two case studies. Physics and Chemistry of the Earth, 36:241-252.

Montagner F, Billat V, Bélanger S (2003) MERIS ATBD 2.13 - Sun glint flag algorithm, issue 4,revision 2

Mueller, N., Lewis, A., Roberts, D., Ring, S., Melrose, R., Sixsmith, J., Lym- Burner, L., McIntyre, A., Tan, P., Curnow, S., and Ip, A. (2016). Water observations from space: Mapping surface water from 25 years of Landsat imagery across Australia. Remote Sensing of Environment, 174:341-352.

Pulvirenti, L., Pierdicca, N., Chini, M., and Guerriero, L. (2011) An algorithm for operational flood mapping from Synthetic Aperture Radar (SAR) data using fuzzy logic, Nat. Hazards Earth Syst. Sci., 11, 529-540, doi:10.5194/nhess-11-529-2011.

Rabus, B., Eineder, M., Roth, A. andBamler, R.(2003). The shuttle radar topography mission- a new class of digital elevation models acquired by spaceborne radar, Photogramm. Rem. Sens., v. 57, p. 241-262.

Rouse, J.W, Haas, R.H., Scheel, J.A., and Deering, D.W. (1974). Monitoring Vegetation Systems in the Great Plains with ERTS,Proceedings, 3rd Earth Resource Technology Satellite (ERTS) Symposium, vol. 1, p. 48-62.

Schumann, G.,Hostache, R.,Puech,C.,Hoffmann,L.,Matgen,P., Pappenberger, F.&Pfister, L. (2007).High-Resolution 3-D Flood Information From Radar Imagery for Flood Hazard Management. IEEE Transactions on Geoscience and Remote Sensing, 45, 1715-1725.

Schroeder, W., Prins, E., Giglio, L., Csiszar,I., Schmidt, C.,Morisette, J., Morton, D.(2008).Validation of GOES and MODIS active fire detection products using ASTER and ETM+ data, Remote Sensing of Environment, 112 (2008) 2711–2726

Sellers, P. J. (1985).Canopy reflectance, photosynthesis, and transpiration, International Journal of Remote Sensing, 6, 1335-1372

Sheng, Y. & Xiao, Q. (1994). Water Identification in Cloud-contaminated NOAA/AVHRRImagery, Remote Sensing of Environment in China, vol. 9, pp. 247–255

Sheng, Y., Su,Y. & Xiao, Q. (1998). Challenging the cloud-contamination problem in floodmonitoring with NOAA/AVHRR imagery, Photogrammetric Engineering RemoteSens., 64, 191–198

Sheng, Y. & Gong, P. (2001). Quantitative dynamic flood monitoring with NOAA AVHRR, Int. J. Remote Sens., vol. 22, no. 9, pp. 1709–1724

Shepard, M. K., Campbell, B. A., Bulmer,M. H., Farr,T. G., Gaddis, L. R. and Plaut, J. J.(2001). The roughness of natural terrain: A planetary and remote sensing perspective, Journal of Geophysical Research, Vol. 106, NO. El2, Pages 32,777-32,795

Sippel, S. J., Hamilton, S. K., Melack, J. M., and Choudhury, B. J. (1994). Determination of inundation area in the Amazon river floodplain using the SMMR 37 GHz polarization difference. Remote Sensing of Environment, 48 (1), 70–76.

Stefanidis, A., Crooks, A., & Radzikowski, J. (2013). Harvesting Ambient Geospatial Information from Social Media Feeds, Geojournal, 78(2): 319-338.

Sun, D. L., Yu, Y. Y., Zhang, R., Li, S. &Goldberg, M. D. (2012).Towards Operational Automatic Flood Detection Using EOS/MODIS data, Photogrammetric Engineering & Remote Sensing, 78 (6), 637-646

Tachikawa, T., Hato, M., Kaku, M. and Iwasaki, A.(2011). The characteristics of ASTER GDEM version 2, IGARSS, July 2011

Tanaka, M., Sugimura, T., Tanaka, S., and Tamai, N. (2003). Flood drought cycle of Tonle Sap and Mekong Delta area observed by DMSP-SSM/I. International Journal of Remote Sensing, 24 (7), 1487–1504.

Thompson, R. J., Oosterom, P.V.,Zlatanova,S.,Giesen, N. V. D. and Goulevitch,B. (2011). Monitoring the Extent of Flooding – Based on a Case Study in Queensland, the International Archives of the Photogrammetry, Remote Sensing and Spatial Information Sciences, Vol. 34, Part XXX

Ticehurst, C., Guerschman, J.P., Chen, Y. (2014). The strengths and limitations in using the daily MODIS open water likelihood algorithm for identifying flood events. Remote Sensing 6 (12), 11791-11809

Ticehurst, C., Dutta, D., Karim, F., Petheram, C., Guerschman, J.P. (2015). Improving the accuracy of daily MODIS OWL flood inundation mapping using hydrodynamic modelling. Natural Hazards 78 (2), 803-820

Tsugawa, R. and James, B (2011). Joint Polar Satellite System (JPSS) VIIRS Snow Cover Algorithm Theoretical Basis Document, NPOESS Common Data Format Control Book – External Volume 5 Metadata,D34862-05

Tulbure, Mirela G.; Broich, Mark; Stehman, Stephen V.; et al. (2016) Surface water extent dynamics from three decades of seasonally continuous Landsat time series at subcontinental scale in a semi-arid region. Remote Sensing of Environment, Vol.178,142-157

Wang,Y.,Colby,J. D. &Mulcahy, K. A.(2002). An efficient method for mapping flood extent in a coastal floodplain using Landsat TM and DEM data. International Journal of Remote Sensing, 23:18, 3681-3696

Wiesnet, D.R., McGinnis,D.V. & Pritchard, J.A. (1974). Mapping of the 1973 Mississippi river floods by the NOAA-2 Satellite, Water Resources Bulletin, 10(5), 1040-1049

Xian, G., Homer, C., and Fry, J., (2009). Updating the 2001 National Land Cover Database land cover classification to 2006 by using Landsat imagery change detection methods. Remote Sensing of Environment, 113, 1133-1147

Xiao, X.G., Shen, Z.X.,and Qin, X. G. (2001). Assessing the potential of VEGETATION sensor data for mapping snow and ice cover: a Normalized Difference Snow and Ice Index, International Journal of remote sensing, 2001, vol. 22, no. 13, 2479–2487

Weng, F., Yang, H., and Zou, X. (2013). On Convertibility from antenna to sensor brightness temperature for ATMS. IEEE Geophysical Research Letters, 10 (4), 771-775.

Zhang Y. X., Zhang L.J., Huang Y. F., Rong, Z. G., Hu, X. Q., Liu, J.J. and Zhang, G. S. (2008). Spectral Data Sets for Satellite Calibration Site and Typical Earth Objects, M., China Meteorological Press, ISBN: 978-7-5029-4422-3

Zheng, W., Liu, C., Wang, Z. X, and Xin, Z. B. (2008). Flood and waterlogging monitoring over Huaihe River Basin by AMSR-E data analysis. China Geographic Science, 18 (3), 262-267.